

MULTIWAVELENGTH OBSERVATIONS OF GRB 050820A: AN EXCEPTIONALLY ENERGETIC EVENT FOLLOWED FROM START TO FINISH

S. B. CENKO,¹ M. KASLIWAL,² F. A. HARRISON,¹ V. PAL'SHIN,³ D. A. FRAIL,⁴ P. B. CAMERON,² E. BERGER,^{5,6,7}
D. B. FOX,⁸ A. GAL-YAM,^{2,7} S. R. KULKARNI,² D.-S. MOON,^{1,9} E. NAKAR,¹⁰ E. O. OFEK,² B. E. PENPRASE,¹¹
P. A. PRICE,¹² R. SARI,¹⁰ B. P. SCHMIDT,¹³ A. M. SODERBERG,² R. APTEKAR,³ D. FREDERIKS,³
S. GOLENETSKII,³ D. N. BURROWS,⁸ R. A. CHEVALIER,¹⁴ N. GEHRELS,¹⁵
P. J. MCCARTHY,⁵ J. A. NOUSEK,⁸ AND T. PIRAN¹⁶

Received 2006 May 18; accepted 2006 August 2

ABSTRACT

We present observations of the unusually bright and long γ -ray burst GRB 050820A, one of the best sampled broadband data sets in the *Swift* era. The γ -ray light curve is marked by a soft precursor pulse some 200 s before the main event; the lack of any intervening emission suggests that it is due to a physical mechanism distinct from the GRB itself. The large time lag between the precursor and the main emission enabled simultaneous observations in the γ -ray, X-ray, and optical bandpasses, something only achieved for a handful of events to date. While the contemporaneous X-rays are the low-energy tail of the prompt emission, the optical does not directly track the γ -ray flux. Instead, the early-time optical data appear consistent with the forward shock synchrotron peak passing through the optical and are therefore likely the beginning of the afterglow. On hour timescales after the burst, the X-ray and optical light curves are inconsistent with an adiabatic expansion of the shock into the surrounding region, but rather indicate that there is a period of energy injection. Observations at late times allow us to constrain the collimation angle of the relativistic outflow to $6^\circ.8 \lesssim \theta \lesssim 9^\circ.3$. Our estimates of both the kinetic energy of the afterglow ($E_{\text{KE}} = 5.2^{+7.9}_{-4.1} \times 10^{51}$ ergs) and the prompt γ -ray energy release ($E_\gamma = 7.5^{+6.7}_{-2.4} \times 10^{51}$ ergs) make GRB 050820A one of the most energetic events for which such values could be determined.

Subject headings: gamma rays: bursts — X-rays: individual (GRB 050820A)

1. INTRODUCTION

With the discovery of the cosmological nature of γ -ray bursts (GRBs) in 1997 (Metzger et al. 1997), astronomers were suddenly forced to explain the enormous isotropic energy release of these distant explosions. Some of the most energetic events, such as GRB 990123, seemingly released enough energy in the prompt

γ -rays ($E_{\gamma,\text{iso}} = 1.2 \times 10^{54}$ ergs; Briggs et al. 1999) to rival the rest mass of a neutron star. Furthermore, broadband modeling of the best sampled events has shown that a comparable amount of energy remains in the shock, powering the long-lived X-ray, optical, and radio afterglow (see, e.g., Panaitescu & Kumar 2001; Yost et al. 2003).

The hypothesis that GRBs are aspherical explosions (Rhoads 1999), supported by the appearance of achromatic “jet” breaks in a large number of afterglow light curves (Sari et al. 1999), proved to be a turning point. With typical opening angles of a few degrees, the true energy release from most GRBs is $\sim 10^{51}$ ergs, on par with that of a supernova (SN). This realization enabled the discovery of a standard energy reservoir for the collimation-corrected prompt energy (Frail et al. 2001) and kinetic energy of the afterglow (Berger et al. 2003a). GRBs are now considered promising standard candle candidates, with the hope of Hubble diagrams out to $z \approx 6$ offering complementary constraints to Type Ia SNe on the cosmology of our universe (Firmani et al. 2006; Dai et al. 2004; cf. Friedman & Bloom 2005).

Launched in 2004 November, the *Swift* Gamma-Ray Burst Explorer (Gehrels et al. 2004) was designed to position GRBs, disseminate accurate coordinates to ground-based observatories in real time, and follow the UV and X-ray afterglows from minutes to days after the event. In only a year of full operation, *Swift* has brought about a number of fundamental advances in the GRB field, including the discovery of the first X-ray (GRB 050509b; Gehrels et al. 2005) and near-infrared (GRB 050724; Berger et al. 2005) afterglows of a short-hard burst, the detection of the high-redshift burst ($z = 6.3$) GRB 050904 (Haislip et al. 2006; Cusumano et al. 2006), and the ability to measure broadband light curves starting shortly after, and in a few cases even during, the γ -ray event itself.

¹ Space Radiation Laboratory, California Institute of Technology, MS 220-47, Pasadena, CA 91125.

² Division of Physics, Mathematics, and Astronomy, California Institute of Technology, MS 105-24, Pasadena, CA 91125.

³ Ioffe Physico-Technical Institute, 26 Polytekhnicheskaya, St. Petersburg 194021, Russia.

⁴ National Radio Astronomy Observatory, P.O. Box O, 1003 Lopezville Road, Socorro, NM 87801.

⁵ Observatories of the Carnegie Institute of Washington, 813 Santa Barbara Street, Pasadena, CA 91101.

⁶ Princeton University Observatory, Peyton Hall, Ivy Lane, Princeton, NJ 08544.

⁷ Hubble Fellow.

⁸ Department of Astronomy and Astrophysics, Pennsylvania State University, 525 Davey Laboratory, University Park, PA 16802.

⁹ Robert A. Millikan Fellow.

¹⁰ Theoretical Astrophysics, California Institute of Technology, MS 130-33, Pasadena, CA 91125.

¹¹ Department of Physics and Astronomy, Pomona College, 610 North College Avenue, Claremont, CA 91711.

¹² Institute for Astronomy, University of Hawaii, 2680 Woodlawn Drive, Honolulu, HI 96822.

¹³ Research School of Astronomy and Astrophysics, Australian National University, Mount Stromlo Observatory, Cotter Road, Weston Creek, Canberra ACT 2611, Australia.

¹⁴ Department of Astronomy, University of Virginia, P.O. Box 3818, Charlottesville, VA 22903.

¹⁵ NASA Goddard Space Flight Center, Greenbelt, MD 20771.

¹⁶ Racah Institute of Physics, Hebrew University, Jerusalem 91904, Israel.

Despite these advances, measuring the bolometric fluences of *Swift* events has proved challenging, for a number of reasons. First, the limited energy range of the *Swift* Burst Alert Telescope (BAT; Barthelmy et al. 2005) means that *Swift* can accurately characterize only the softest GRB spectra. Second, few *Swift* events have shown conclusive signs of a jet break, leaving geometric corrections highly uncertain. Finally, the X-ray light curves of *Swift* afterglows have shown both bright flares (Burrows et al. 2005a) and slow decays (Nousek et al. 2006). Both behaviors have been attributed to late-time ($t \gg t_{\text{GRB}}$) energy injection and at times have rivaled the energy release of the prompt γ -ray emission (see, e.g., Falcone et al. 2006).

On 2005 August 20 UT, the BAT detected and localized the unusually bright and long GRB 050820A, a truly rare burst in the *Swift* sample. The γ -ray light curve is marked by a soft pulse of emission preceding the main event by over 200 s. The main emission was bright enough to be detected by the *Konus-Wind* instrument, providing a γ -ray spectrum extending beyond 1 MeV, as well as continuous coverage over the entire ~ 600 s burst duration.

Since *Swift* triggered on the precursor, both space- and ground-based facilities were able to image the transient during the bulk of the prompt emission. Such contemporaneous multiwavelength observations have only been achieved for a handful of bursts to date. The bright X-ray ($F_\nu \sim 0.7$ mJy) and optical ($R \sim 14.5$ mag) afterglows made it possible to study the evolution of the afterglow for weeks after the burst, providing one of the most detailed broadband light curves in the *Swift* era. Finally, late-time *Hubble Space Telescope* (*HST*) observations allowed us to constrain the jet break time and hence the geometry of the outflow. Even after applying the collimation correction, we find that GRB 050820A is an exceptionally energetic event.

Our work proceeds as follows: In § 2 we outline our broadband observations of GRB 050820A, beginning with the high-energy prompt emission and followed by the X-ray, optical, and radio afterglow. We find that the afterglow data are incompatible with the standard model of synchrotron radiation from a single, highly relativistic shock expanding adiabatically into the surrounding medium (Sari et al. 1998). Instead, in § 3 we use power-law fits ($F_\nu \propto t^{-\alpha} \nu^{-\beta}$) to model the afterglow, dividing the burst into segments based on noticeable temporal breaks in the X-ray and optical light curves. This analysis allows us to investigate the early broadband light curve (§§ 4.1 and 4.2), late-time ($t \gg t_{\text{GRB}}$) energy injection in the forward shock (§ 4.3), the structure of the circumburst medium (§ 4.4), and the geometry and energetics of the event (§ 4.5).

Throughout this work we adopt a standard cosmology with $H_0 = 71$ km s $^{-1}$ Mpc $^{-1}$, $\Omega_M = 0.73$, and $\Omega_\Lambda = 0.27$. We also make use of the notation $Q_X \equiv 10^X \times Q$. Unless otherwise noted, all errors quoted are 90% confidence limits.

2. OBSERVATIONS AND DATA REDUCTION

In this section we present our broadband observations of GRB 050820A, which span the spectral range from γ -rays to radio frequencies and extend in time out to 61 days after the burst. We include an independent analysis of the *Swift* BAT data set, as well as the complete light curve and spectrum from the *Konus-Wind* instrument (Aptekar et al. 1995), which, unlike the BAT, was able to observe GRB 050820A over its entire duration (§ 2.1). In § 2.2 we provide an analysis of the *Swift* X-Ray Telescope (XRT; Burrows et al. 2005b) data, with afterglow detections out to 2 weeks after the event. We present contemporaneous optical data from the automated Palomar 60 inch (1.5 m) telescope (P60; Cenko et al. 2006) and the *Swift* Ultra-Violet/Optical Telescope (UVOT; Roming et al. 2005), supplemented by late-time

images taken with the 9.2 m Hobby-Eberly Telescope (HET) and *HST* (§ 2.3). Finally, we monitored GRB 050820A in the radio with the Very Large Array¹⁷ (VLA) beginning only hours after the burst and continuing for approximately 2 months (§ 2.4).

2.1. γ -Ray Observations

2.1.1. *Swift* BAT

At 06:34:53 on 2005 August 20 UT,¹⁸ the BAT triggered and located GRB 050820A (*Swift* trigger 151207; Page et al. 2005b). The initial location calculated on board was a 4' error circle centered at $\alpha = 22^{\text{h}}29^{\text{m}}35^{\text{s}}.9$, $\delta = +19^\circ 11' 14''.2$ (J2000.0). Cummings et al. (2005a) describe a multi-peaked light curve ($t_{90} = 26 \pm 2$ s) with clear spectral evolution (hard to soft) within each peak.

Following the report of additional high-energy emission from the *Konus-Wind* instrument (Pal'shin & Frederiks 2005; see § 2.1.2), the BAT team reanalyzed their full light curve and found evidence of a much stronger, harder episode of emission from GRB 050820A (Cummings et al. 2005b). Unfortunately, the satellite entered the South Atlantic Anomaly (SAA) approximately 240 s after the burst trigger; thus, estimates of the properties of this second phase are highly uncertain.

Here we have independently analyzed the BAT data from GRB 050820A. We have extracted the 15–350 keV light curve in 1 s timing bins using software tools from the *Swift* data analysis package.¹⁹ The result is shown in Figure 1a. In addition, we have extracted spectra for the two periods of high-energy emission covered by the BAT data (peaks A and B; see § 2.1.2). We then fitted these spectra to a power-law distribution of energies ($dN/dE \propto E^{-\Gamma}$). We find evidence for strong spectral evolution between these two intervals, as the second peak is significantly harder than the first. The results of this analysis are shown in Table 1.

2.1.2. *Konus-Wind*

The main part of GRB 050820A triggered *Konus-Wind* at T_{KW} of 06:39:14.512 UT, 257.948 s after the BAT trigger (taking into account the 3.564 s propagation delay from *Swift* to *Wind*). It was detected by the S2 detector, which observes the north ecliptic hemisphere; the incident angle was 63°.2. Count rates are continuously recorded by *Konus-Wind* in three energy bands: G1 (18–70 keV), G2 (70–300 keV), and G3 (300–1150 keV). Data collected in this “waiting mode” are acquired in 2.944 s timing bins. The time history recorded in the three energy ranges can be considered a continuous three-channel spectrum.

Immediately following the *Konus-Wind* trigger, the instrument began simultaneously collecting data in “trigger” mode, as well. From T_{KW} to $T_{\text{KW}} + 491.776$ s, 64 spectra, each composed of 101 energy channels ranging from 18 keV to 14 MeV, were accumulated. The time resolution of these “trigger mode” spectra varies from 64 ms to 8.192 s and is determined by an automated onboard algorithm based on count rate. Data were then processed using standard *Konus-Wind* analysis tools and spectra were fitted with XSPEC.

¹⁷ The National Radio Astronomy Observatory is a facility of the National Science Foundation operated under cooperative agreement by Associated Universities, Inc.

¹⁸ It is customary to refer to the burst trigger time as T_0 , for it is assumed to coincide with the beginning of the prompt emission. Given the unique nature of the high-energy emission from GRB 050820A, we undertake a more detailed study to determine exactly when the prompt emission began (i.e., T_0) in § 4.1. Times measured with reference to the *Swift* trigger time are referred to as t_{BAT} throughout the remainder of this work.

¹⁹ Part of NASA's High Energy Astrophysics Software package; see <http://heasarc.gsfc.nasa.gov/docs/software/lheasoft>.

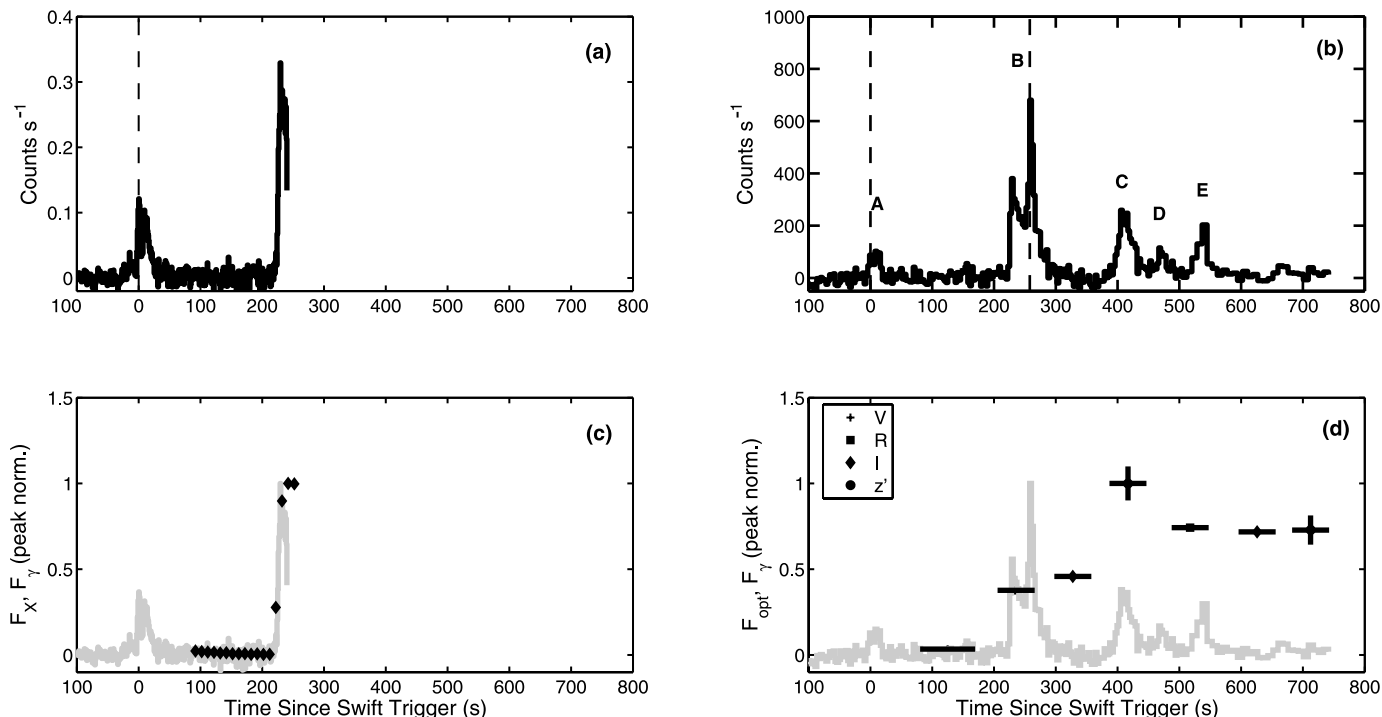


FIG. 1.—Early broadband emission from GRB 050820A. (a) *Swift* BAT light curve extracted from 15 to 350 keV in 1 s bins. The dashed vertical line is the time of *Swift* trigger, 06:34:53 on 2005 August 20 UT (t_{BAT}). While the second, brighter period of emission is clearly visible, *Swift* entered the SAA approximately 240 s after t_{BAT} , effectively terminating the observations. (b) *Konus-Wind* light curve extracted from 18 to 1150 keV. The five peaks visible in the *Konus-Wind* light curve are labeled A–E and defined in Table 2. The left dashed vertical line shows the *Swift* trigger time, while the right dashed line shows the *Konus-Wind* trigger time, t_{KW} , 258 s later. The portion of the light curve covered by the BAT comprises only a small fraction of the total γ -ray emission. (c) Contemporaneous *Swift* XRT observations (black filled diamonds) overlaid on the BAT light curve. The X-ray data nicely track the γ -ray emission. (d) Contemporaneous UVOT and P60 optical data overlaid on the *Konus-Wind* light curve. Unlike the X-ray, the optical is not a good trace of γ -ray emission.

At least five pulses are evident in the *Konus-Wind* light curve (labeled A–E; see Fig. 1b and Table 2). Peak A, which generated the BAT trigger, appears to be a weak precursor. Figure 2 shows the three-channel light curve of GRB 050820A, as well as the hardness ratios. With the exception of the precursor (peak A), the burst shows an overall hard-to-soft evolution over the entire burst duration, as well as within some of the individual peaks (B and C).

The spectra of individual pulses are well fitted by a cutoff power-law model: $dN/dE \propto E^{-\alpha} \exp[-(2-\alpha)E/E_p]$; here α is the photon index and E_p is the peak energy of the νF_ν spectrum (see, e.g., § 4.2). Fitting the overall *Konus-Wind* trigger mode spectrum, accumulated from $0 < t_{\text{KW}} < 295$ ($258 < t_{\text{BAT}} < 553$),²⁰ in the 18–2000 keV range yields $\alpha = 1.41^{+0.25}_{-0.31}$ and a peak energy $E_p = 271^{+359}_{-91}$ keV ($\chi_r^2 = 0.74$, 62 dof).

However, in examining the full *Konus-Wind* light curve (Fig. 1b), it is clear that the above time interval does not include

²⁰ After this time only a weak tail is seen in the G1 band up to $t_{\text{BAT}} \approx 730$ s; this tail contains less than 5% of the total burst fluence.

TABLE 1
SPECTRAL PROPERTIES OF BAT γ -RAY EMISSION

Time Interval, t_{BAT} (s)	Γ	χ_r^2/dof
–17 to 22.....	1.74 ± 0.08	1.07/75
217–241.....	1.07 ± 0.06	0.95/76

NOTES.—Spectra were fitted to a power-law model of the form $dN/dE \propto E^{-\Gamma}$. Errors reported are 90% confidence limits.

a sizable fraction of the γ -ray emission. To derive the spectral parameters of the time-integrated spectrum over the main part of the GRB (peaks B–E), we simultaneously fitted the three-channel *Konus-Wind* spectrum accumulated from $-33 < t_{\text{KW}} < 0$ and the overall multichannel spectrum. We find $\alpha = 1.12^{+0.13}_{-0.15}$ and a peak energy $E_p = 367^{+95}_{-62}$ keV ($\chi_r^2 = 0.99$, 64 dof). Not surprisingly, the peak energy increased significantly, as the beginning of peak B was the hardest portion of the entire burst. We consider this fit the most accurate estimate of the high-energy spectral properties of GRB 050820A.

The fluence and peak flux for each individual episode are shown in Table 2. The total fluence received from GRB 050820A from 20 to 1000 keV (observer frame) was $5.27^{+1.58}_{-0.69} \times 10^{-5}$ ergs cm^{-2} (90% confidence limit).

TABLE 2
PROPERTIES OF *Konus-Wind* γ -RAY LIGHT CURVE

Peak ID	Time Interval, t_{BAT} (s)	Fluence ^a (10^{-6} ergs cm^{-2})	Peak Flux (10^{-7} ergs cm^{-2} s^{-1})
A.....	–4.3 to 19.3	2.77	1.7
B.....	222.4–282.8	28.7	13
C.....	397.5–430.2	10.2	4.3
D.....	454.8–479.4	3.20	1.9
E.....	520.4–544.9	4.93	2.6
Total.....	–4.3 to 544.9	$52.7^{+15.8}_{-6.9}$...

^a The fluence was extracted from the 20–1000 keV energy range (observer frame) assuming a cutoff power-law spectrum of the form $dN/dE \propto E^{-\alpha} \exp[-(2-\alpha)E/E_p]$. Errors reported are 90% confidence limits (see § 2.1.2 for further details).

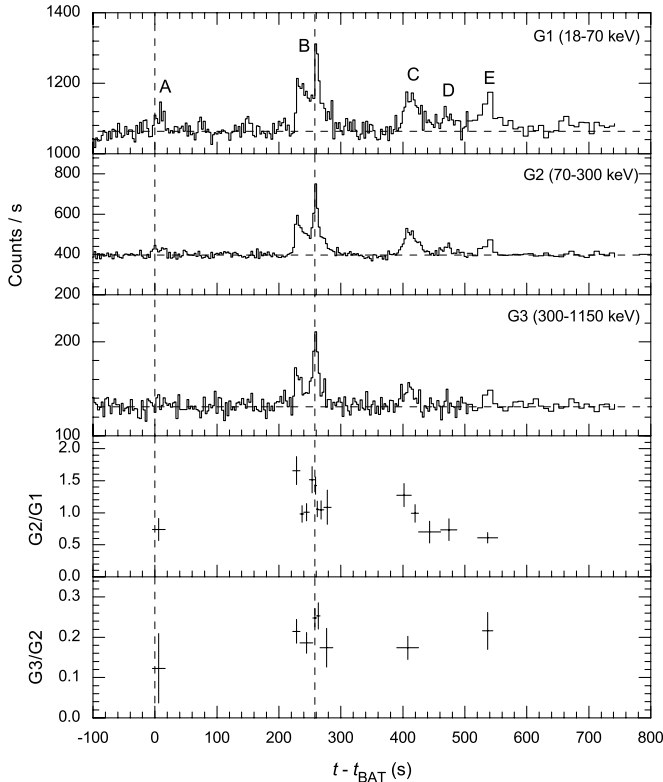


FIG. 2.—Spectral evolution of GRB 050820A. The top three panels show the *Konus-Wind* light curve divided into three energy bands: G1 \equiv 18–70 keV, G2 \equiv 70–300 keV, and G3 \equiv 300–1050 keV. The bottom two panels show the resulting hardness ratios: G2/G1 and G3/G2. Background levels are indicated with horizontal dashed lines. The vertical dashed lines denote the BAT (T_{BAT}) and *Konus-Wind* (T_{KW}) trigger times. With the notable exception of the precursor, the burst shows an overall hard-to-soft evolution, both over the entire duration and within individual bright peaks (B and C).

2.2. X-Ray Observations

The *Swift* XRT began observations of GRB 050820A 88 s after the burst trigger. A bright, fading X-ray source was detected by the automated onboard processing routine at $\alpha = 22^{\text{h}}29^{\text{m}}37^{\text{s}}.8$, $\delta = +19^{\circ}33'32''.7$ (7'' error radius) and reported in real time (Page et al. 2005b). Data were taken in window timing mode until ~ 1.29 hr after the burst, when, due to the decreased count rate, photon counting mode was automatically initiated.

Here we have independently processed and reduced the XRT data from GRB 050820A (for a previous analysis of the early-time X-ray data, see O’Brien et al. 2006). To reduce the X-ray data, we used the software tools available from the *Swift* Data Center. We followed standard reduction steps, except for taking measures to mitigate the effects of pulse pileup in our spectral analysis. During the steep rise in the X-ray light curve at $t_{\text{BAT}} \approx 220$ s, the XRT count rate exceeds the 200 counts s^{-1} at which pileup can affect the detector response (Romano et al. 2006). For this segment, we removed the central 2 pixels from the point-source image. At the beginning of photon counting mode, we removed the central 4 pixels of the photon counting mode image for our spectral analysis, again in order to mitigate the effect of pulse pileup (Vaughan et al. 2006).

We fitted the X-ray spectrum for phases 1a, 1b, and 2 separately (see § 3 for a full discussion of the division of the X-ray light curve into phases). We used an absorbed power-law model and fitted both with the column fixed to the Galactic value ($n_{\text{H,Gal}} = 5.0 \times 10^{20} \text{ cm}^{-2}$; Dickey & Lockman 1990), as well as with the column floating. For phase 1a, the best-fit column is consistent with $n_{\text{H,Gal}}$,

and there is little difference between fits with the column floating and fixed. For both phases 1b and 2 we find acceptable fits with fixed column; however, the best-fit columns are $(1.5 \pm 0.23) \times 10^{21}$ and $(1.3 \pm 0.09) \times 10^{21} \text{ cm}^{-2}$, respectively. Therefore, we find marginal evidence for absorption in excess of the Galactic value (cf. Page et al. 2005a).

The results of our analysis of the X-ray light curve of GRB 050820A are shown in Table 3. For the discussion below we adopt the spectral fits in Table 4. These were used to scale the binned count rates to fluxes and flux density at a nominal energy of 5 keV.

2.3. Optical Observations

2.3.1. Palomar 60 inch Telescope

The automated P60 responded to GRB 050820A and began a preprogrammed sequence of observations starting 3.43 minutes after the *Swift* trigger. The system is equipped with an optical CCD with a pixel scale of $0''.378 \text{ pixel}^{-1}$. Images were taken in the Kron *R* and *I* and Gunn *g* and *z* filters. All P60 images are processed with standard IRAF (Tody 1986) routines by an automated reduction pipeline in real time. Manual inspection of the first images revealed a bright variable source inside the XRT error circle at $\alpha = 22^{\text{h}}29^{\text{m}}38^{\text{s}}.11$, $\delta = +19^{\circ}33'37''.1$ (see Fig. 3). This position was promptly reported as the afterglow of GRB 050820A (Fox & Cenko 2005), allowing others to obtain high-resolution spectroscopy of the afterglow (Prochaska et al. 2005). We continued to monitor the afterglow of GRB 050820A with P60 for the following seven nights, until it was too faint for quantitative photometry.

Optical photometry of the afterglow was complicated by the presence of two nearby objects: one $R \sim 20.2$ mag star located $4''.0$ southwest of the afterglow, and a fainter $R \sim 21.3$ mag object located only $2''.9$ northeast of the afterglow (see Fig. 3, *right panel*). On some nights of poor seeing, the FWHM of our point-spread function (PSF) was larger than $2''.0$. We have therefore performed PSF-matched image subtraction using the common PSF method (CPM) technique of Gal-Yam et al. (2004) on our optical data. Errors were estimated by placing five artificial stars with flux equivalent to the afterglow in locations with similar background contamination. In addition, we have also used aperture photometry (DAOPHOT) to extract the afterglow flux. On the first night, the afterglow was bright enough to be well detected in either single images or short co-additions (≤ 360 s). For these images, both nearby sources were below our detection limit. Results from aperture photometry and image subtraction were therefore consistent. We quote our aperture photometry results for these data, as image defects from imperfect PSF subtraction seemed to artificially inflate these errors. However, on subsequent nights the afterglow flux was either near or below the level of these nearby objects, and we therefore report results from our image subtraction technique.

Photometric calibration was performed relative to 20 field stars provided in Henden (2005). Kron *R* is similar to Cousins *R* (R_C) and was treated as identical for photometric calibration of these images. Magnitudes from the standard Johnson/Cousins system were transformed to Gunn *g* using the empirical relation from Kent (1985). We found, however, a better correlation between our *i*-band filter and the Cousins *I* (I_C) filter than from the transformation to Gunn *i* provided in Thuan & Gunn (1976). We therefore use I_C in the remainder of this work. For the Gunn *z* filter, we used the Two Micron All Sky Survey (2MASS; Skrutskie et al. 2006) catalog and the optical photometry provided by Henden (2005) to interpolate the spectral energy distributions (SEDs) of 10 sources

TABLE 3
XRT OBSERVATIONS OF GRB 050820A

Mean Observation Date (2005 UT)	t_{BAT} (s)	Duration (s)	Spectral Index (β)	2–10 keV Flux (10^{-11} ergs cm^{-2} s^{-1})
Aug 20 06:36:25.....	92.0	10.0	0.90	14.9 ± 1.3
Aug 20 06:36:35.....	102.0	10.0	...	12.2 ± 1.2
Aug 20 06:36:45.....	112.0	10.0	...	10.8 ± 1.1
Aug 20 06:36:55.....	122.0	10.0	...	9.8 ± 1.1
Aug 20 06:37:05.....	132.0	10.0	...	7.3 ± 0.9
Aug 20 06:37:15.....	142.0	10.0	...	8.1 ± 1.0
Aug 20 06:37:25.....	152.0	10.0	...	4.8 ± 0.8
Aug 20 06:37:35.....	162.0	10.0	...	4.5 ± 0.8
Aug 20 06:37:45.....	172.0	10.0	...	4.9 ± 0.8
Aug 20 06:37:55.....	182.0	10.0	...	2.5 ± 0.6
Aug 20 06:38:05.....	192.0	10.0	...	4.0 ± 0.7
Aug 20 06:38:15.....	202.0	10.0	...	2.3 ± 0.8
Aug 20 06:38:25.....	212.0	10.0	...	2.4 ± 0.7
Aug 20 06:38:35.....	222.0	10.0	-0.10	175.1 ± 7.9
Aug 20 06:38:45.....	232.0	10.0	...	567.0 ± 14.2
Aug 20 06:38:55.....	242.0	10.0	...	631.3 ± 15.0
Aug 20 06:39:05.....	252.0	10.0	...	629.7 ± 26.5
Aug 20 07:56:43.....	4.910×10^3	250.0	1.20	3.0 ± 0.2
Aug 20 08:00:53.....	5.160×10^3	250.0	...	3.1 ± 0.2
Aug 20 08:05:03.....	5.410×10^3	250.0	...	3.2 ± 0.2
Aug 20 08:09:13.....	5.660×10^3	250.0	...	2.8 ± 0.2
Aug 20 08:13:23.....	5.910×10^3	250.0	...	2.6 ± 0.2
Aug 20 11:41:43.....	1.841×10^4	2.5×10^3	...	1.02 ± 0.05
Aug 20 12:23:23.....	2.091×10^4	2.5×10^3	...	0.9 ± 0.1
Aug 20 13:05:03.....	2.341×10^4	2.5×10^3	...	0.71 ± 0.03
Aug 20 14:28:23.....	2.841×10^4	2.5×10^3	...	0.58 ± 0.03
Aug 20 15:10:03.....	3.091×10^4	2.5×10^3	...	0.51 ± 0.06
Aug 20 15:51:43.....	3.341×10^4	2.5×10^3	...	0.52 ± 0.04
Aug 20 16:33:23.....	3.591×10^4	2.5×10^3	...	0.56 ± 0.06
Aug 20 17:15:03.....	3.841×10^4	2.5×10^3	...	0.47 ± 0.07
Aug 20 17:56:43.....	4.091×10^4	2.5×10^3	...	0.49 ± 0.05
Aug 20 19:20:03.....	4.951×10^4	2.5×10^3	...	0.39 ± 0.08
Aug 21 15:48:01.....	1.196×10^5	1.0×10^4	...	0.18 ± 0.03
Aug 21 18:34:41.....	1.296×10^5	1.0×10^4	...	0.14 ± 0.01
Aug 21 21:21:21.....	1.396×10^5	1.0×10^4	...	0.13 ± 0.02
Aug 22 00:08:01.....	1.496×10^5	1.0×10^4	...	0.10 ± 0.02
Aug 22 02:54:41.....	1.596×10^5	1.0×10^4	...	0.07 ± 0.01
Aug 23 14:30:22.....	2.877×10^5	1.0×10^4	...	0.046 ± 0.006
Aug 23 17:17:02.....	2.977×10^5	1.0×10^4	...	0.050 ± 0.008
Aug 24 18:02:47.....	3.869×10^5	3.5×10^4	...	0.034 ± 0.004
Aug 25 03:46:07.....	4.219×10^5	3.5×10^4	...	0.05 ± 0.01
Aug 27 19:38:46.....	6.518×10^5	1.25×10^5	...	0.022 ± 0.003
Aug 29 06:22:06.....	7.768×10^5	1.25×10^5	...	0.014 ± 0.002
Sep 04 15:45:23.....	1.329×10^6	1.0×10^5	...	$(6.8 \pm 2.5) \times 10^{-3}$
Sep 05 19:32:03.....	1.429×10^6	1.0×10^5	...	$(4.2 \pm 1.5) \times 10^{-3}$
Sep 06 23:18:43.....	1.529×10^6	1.0×10^5	...	$(8.8 \pm 3.3) \times 10^{-3}$

NOTES.—The four phases of the X-ray light curve are shown as follows: phase 1ax is shown in rows 1–13, phase 1bx in rows 14–17, phase 2 in rows 18–32, and phase 3 in rows 33–46 (see § 3.1 for further details). We assumed that the spectral index was constant in each phase to convert count rates to the flux values shown here. We also assumed that the spectral index remained constant from phase 2 to phase 3. All errors quoted are at the 1σ level.

TABLE 4
X-RAY AFTERGLOW SPECTRAL AND TEMPORAL FITS

Phase	$t_{\text{BAT}}^{\text{start}}$ (s)	$t_{\text{BAT}}^{\text{stop}}$ (s)	α	$\chi_r^2(\alpha)/\text{dof}$	β	$\chi_r^2(\beta)/\text{dof}$
1a.....	0	217	2.2 ± 0.3	1.18/11	0.90 ± 0.09	0.63/349
1b.....	217	257	-0.10 ± 0.03	1.02/749
2.....	4.8×10^3	8.7×10^4	0.93 ± 0.03	1.14/29	1.20 ± 0.04	1.00/770
3.....	8.7×10^4	1.7×10^6	1.25 ± 0.07

NOTES.—We separately fitted the X-ray light curves and spectra to power-law models of the form $F_\nu \propto t^{-\alpha}$ and $F_\nu \propto \nu^{-\beta}$, respectively. The temporal decays in phases 2 and 3 were fitted jointly as a broken power law, with the break time as a free parameter. In phase 3, we could not meaningfully constrain the spectral index due to the low count rate. All errors quoted are 90% confidence limits.

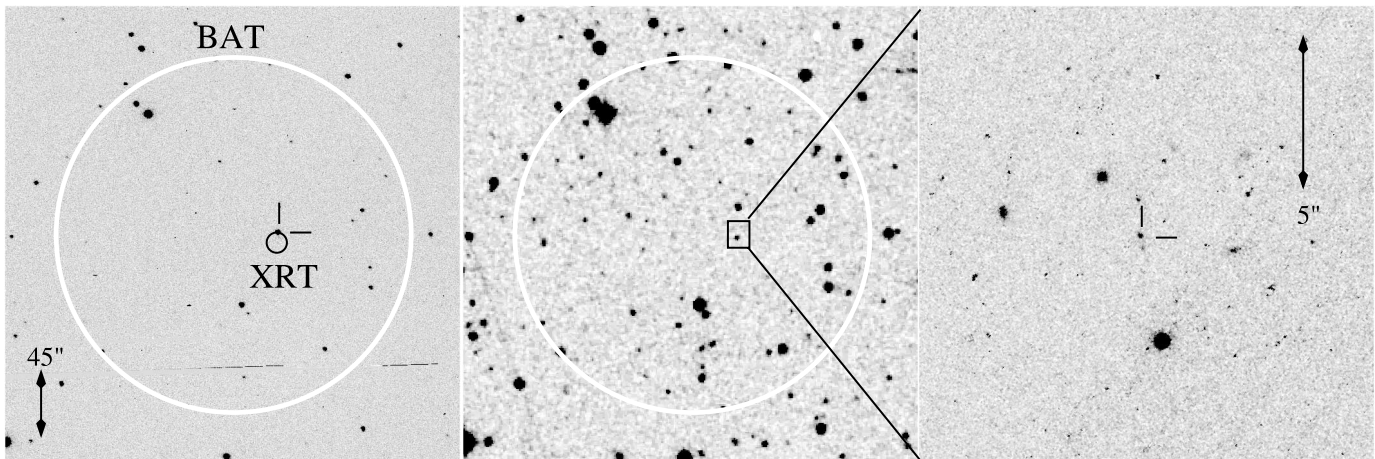


FIG. 3.—*R*-band imaging of the field of GRB 050820A. *Left*: P60 R_C band discovery image of the afterglow of GRB 050820A. The BAT ($2'$ radius, white circle) and XRT ($7''$ radius, black circle) error circles are labeled. The afterglow is identified with the two black tick marks. *Middle*: Second-generation Digitized Sky Survey image of the identical field. The afterglow is not visible in this reference image. *Right*: *HST* F625W image of the afterglow (indicated again with the two black tick marks). The two nearby objects complicating the ground-based photometry are visible (see § 2.3.1 for details). All images are oriented with north up and east to the left.

to the Sloan z' bandpass. Typical rms variations in the calibration sources were 0.03 mag in R_C and I_C , 0.04 mag in g , and 0.15 in z' .

The results of our P60 observations are shown in Table 5. While the expected Galactic extinction in this direction is small [$E(B - V) = 0.044$ mag; Schlegel et al. 1998], we have incorporated it into our results because of the large wavelength range spanned by our observations [$E(U - z') = 0.17$ mag]. Errors quoted are 1σ photometric and instrumental errors summed in quadrature. For this and all other optical data in this work, magnitudes are converted to flux densities using the zero points reported in Fukugita et al. (1995).

2.3.2. *Swift* UVOT

The *Swift* UVOT automatically slewed to the BAT location and began observations only 80 s after the trigger. However, the UVOT also becomes inoperable in the SAA and therefore does not cover the period of the main γ -ray emission.

The *Swift* team reduced the early-time UVOT data and reported detections in the V , B , U , and UVW1 bands (Chester et al. 2005). Here we have independently reduced the U -, B -, and V -band UVOT data following the recipe outlined in Li et al. (2006, see their § 3.6). As a check, we recalculated the B and V zero points with respect to the field stars from Henden (2005). While our zero points are consistent with the ones quoted in Li et al. (2006), we found a much larger scatter (~ 0.10 mag vs. 0.01 mag) that could not be attributable solely to spread in the field stars. We have therefore incorporated the resulting zero-point errors for these data points (as well as a similar value for U band). The results of these observations are shown in Table 5.

2.3.3. *Hobby-Eberly Telescope*

We triggered target-of-opportunity observations on the 9.2 m HET beginning on the night of August 26 UT. Observations were taken in both R_C and I_C filters. A second reference epoch was taken on August 29 UT. Image subtraction was performed on the two epochs to remove contamination from nearby sources (as described in § 2.3.1). Photometric calibration was performed relative to 10 reference objects from Henden (2005), and the absolute calibration was of similar quality to the P60 data set. Our results are reported in Table 5.

2.3.4. *Hubble Space Telescope*

To better constrain the jet break time, as well as to investigate the properties of the host galaxy of GRB 050820A, we triggered our Cycle 14 *HST* program (GO-10551; PI: Kulkarni). Using the Wide Field Channel (WFC) of the Advanced Camera for Surveys (ACS), we imaged the field of GRB 050820A on 2005 September 29 UT ($t_{\text{BAT}} \approx 37$ days) in the F625W (r'), F775W (i'), and F850LP (z') filters (see Fig. 3). A second epoch to study the host galaxy is scheduled for 2006 July, and these results will be reported in a future work.

The *HST* data were processed using the *multidrizzle* routine (Fruchter & Hook 2002) in the *stdas* IRAF package. We used $\text{pixfrac} = 0.8$ and $\text{pixscale} = 1.0$ for the drizzling procedure, resulting in a pixel scale of $0''.05 \text{ pixel}^{-1}$. The astrometry on these images was then tied to a P60 co-addition of all of the R_C band data taken on 2005 August 20 (which is itself tied to the USNO-B1 astrometric grid).

The afterglow is well separated from any nearby objects in the field, and so we have followed the recipe for aperture photometry from Sirianni et al. (2005). As a note of caution, however, flux from an underlying host galaxy could affect the results reported here. Final values for the late-time afterglow flux will require image subtraction of any host galaxy contribution, expected following our July observations. F625W and F775W magnitudes were converted to the R_C and I_C bandpasses using synthetic spectra from Table 22 of Sirianni et al. (2005). The results of our measurements are shown in Table 5.

2.4. *Radio Observations*

In Table 6 we summarize our radio observations of GRB 050820A, spanning 0.1–61 days after the explosion. All observations were conducted with the VLA in standard continuum mode with a bandwidth of 2×50 MHz centered at 4.86, 8.46, or 22.5 GHz. The array was in the C configuration, with an angular resolution of $2''.3$. We used 3C 48 (J0137+331) for flux calibration, while J2212+239 and J2225+213 were used to monitor phase. Data were reduced using standard packages within the Astronomical Image Processing System (AIPS).

3. ANALYSIS

In this section we provide an analysis of the X-ray, optical, and radio light curves and spectra of the afterglow of GRB 050820A.

TABLE 5
OPTICAL OBSERVATIONS OF GRB 050820A

Mean Observation Date (2005 UT)	t_{BAT} (s)	Telescope	Filter	Exposure Time (s)	Magnitude ^a (Vega)	Reference
Aug 20 08:14:47.....	5.994×10^3	UVOT	<i>U</i>	693.3	18.12 ± 0.13	1
Aug 20 12:49:02.....	2.245×10^4	UVOT	<i>U</i>	899.8	19.11 ± 0.14	1
Aug 20 16:01:58.....	3.403×10^4	UVOT	<i>U</i>	899.8	19.40 ± 0.14	1
Aug 20 19:14:54.....	4.560×10^4	UVOT	<i>U</i>	899.8	19.66 ± 0.15	1
Aug 20 22:59:51.....	5.910×10^4	UVOT	<i>U</i>	392.3	19.70 ± 0.18	1
Aug 20 09:36:06.....	1.087×10^4	UVOT	<i>B</i>	899.8	18.79 ± 0.16	1
Aug 20 13:04:10.....	2.336×10^4	UVOT	<i>B</i>	899.8	19.24 ± 0.15	1
Aug 20 16:17:05.....	3.493×10^4	UVOT	<i>B</i>	897.3	19.74 ± 0.16	1
Aug 20 19:30:02.....	4.651×10^4	UVOT	<i>B</i>	899.8	19.87 ± 0.16	1
Aug 21 23:30:41.....	1.473×10^5	RTT150	<i>B</i>	1800.0	21.28 ± 0.06	2
Aug 22 22:58:17.....	2.318×10^5	RTT150	<i>B</i>	7860.0	22.05 ± 0.06	3
Aug 23 22:09:05.....	3.153×10^5	RTT150	<i>B</i>	5400.0	22.38 ± 0.08	3
Aug 20 07:01:53.....	1.620×10^3	P60	<i>g</i>	120.0	16.27 ± 0.04	1
Aug 20 07:12:35.....	2.262×10^3	P60	<i>g</i>	120.0	16.65 ± 0.04	1
Aug 20 07:23:24.....	2.911×10^3	P60	<i>g</i>	120.0	16.92 ± 0.05	1
Aug 20 08:04:47.....	5.394×10^3	P60	<i>g</i>	360.0	17.59 ± 0.05	1
Aug 20 08:29:42.....	6.889×10^3	P60	<i>g</i>	360.0	17.87 ± 0.06	1
Aug 20 08:54:50.....	8.397×10^3	P60	<i>g</i>	360.0	18.11 ± 0.06	1
Aug 20 09:33:18.....	1.070×10^4	P60	<i>g</i>	720.0	18.29 ± 0.06	1
Aug 20 10:43:25.....	1.491×10^4	P60	<i>g</i>	720.0	18.36 ± 0.06	1
Aug 20 11:39:32.....	1.828×10^4	P60	<i>g</i>	720.0	18.59 ± 0.09	1
Aug 20 06:36:58.....	125.0	UVOT	<i>V</i>	89.0	18.18 ± 0.20	1
Aug 20 07:52:58.....	4.685×10^3	UVOT	<i>V</i>	99.8	17.20 ± 0.13	1
Aug 20 10:04:28.....	1.258×10^4	UVOT	<i>V</i>	337.0	18.16 ± 0.12	1
Aug 20 11:12:34.....	1.666×10^4	UVOT	<i>V</i>	899.8	18.39 ± 0.09	1
Aug 20 14:25:30.....	2.824×10^4	UVOT	<i>V</i>	899.8	18.86 ± 0.11	1
Aug 20 17:38:26.....	3.981×10^4	UVOT	<i>V</i>	899.8	19.35 ± 0.12	1
Aug 20 21:03:50.....	5.214×10^4	UVOT	<i>V</i>	899.8	19.14 ± 0.11	1
Aug 21 16:09:34.....	1.209×10^5	UVOT	<i>V</i>	899.8	20.24 ± 0.19	1
Aug 21 19:22:30.....	1.325×10^5	UVOT	<i>V</i>	899.8	20.40 ± 0.22	1
Aug 20 06:38:49.....	236.0	P60	R_C	60.0	15.39 ± 0.04	1
Aug 20 06:43:31.....	518.0	P60	R_C	60.0	14.65 ± 0.02	1
Aug 20 06:48:25.....	812.0	P60	R_C	60.0	15.06 ± 0.03	1
Aug 20 06:53:59.....	1.146×10^3	P60	R_C	120.0	15.42 ± 0.02	1
Aug 20 07:04:34.....	1.781×10^3	P60	R_C	120.0	16.05 ± 0.03	1
Aug 20 07:15:19.....	2.426×10^3	P60	R_C	120.0	16.39 ± 0.02	1
Aug 20 07:32:13.....	3.440×10^3	P60	R_C	360.0	16.77 ± 0.02	1
Aug 20 08:12:58.....	5.885×10^3	P60	R_C	360.0	17.32 ± 0.04	1
Aug 20 08:38:05.....	7.392×10^3	P60	R_C	360.0	17.48 ± 0.04	1
Aug 20 08:46:53.....	7.920×10^3	PROMPT-5	R_C	660.0	17.52 ± 0.09	4
Aug 20 09:03:19.....	8.906×10^3	P60	R_C	360.0	17.69 ± 0.04	1
Aug 20 09:28:50.....	1.044×10^4	P60	R_C	360.0	17.85 ± 0.04	1
Aug 20 10:00:44.....	1.235×10^4	P60	R_C	360.0	17.78 ± 0.04	1
Aug 20 10:38:59.....	1.465×10^4	P60	R_C	360.0	17.97 ± 0.04	1
Aug 20 11:05:54.....	1.626×10^4	P60	R_C	360.0	18.01 ± 0.04	1
Aug 20 11:33:14.....	1.790×10^4	P60	R_C	360.0	18.03 ± 0.04	1
Aug 20 12:02:31.....	1.966×10^4	P60	R_C	360.0	18.16 ± 0.05	1
Aug 21 00:37:53.....	6.498×10^4	RTT150	R_C	900.0	19.36 ± 0.01	2
Aug 21 04:16:53.....	7.812×10^4	PROMPT-5	R_C	5370.0	19.94 ± 0.31	4
Aug 22 00:00:05.....	1.491×10^5	RTT150	R_C	1800.0	20.26 ± 0.05	2
Aug 22 07:17:03.....	1.753×10^5	P60	R_C	6840.0	20.51 ± 0.11	1
Aug 22 23:00:41.....	2.319×10^5	RTT150	R_C	3900.0	20.90 ± 0.03	3
Aug 23 08:06:11.....	2.647×10^5	P60	R_C	8400.0	20.89 ± 0.10	1
Aug 23 22:18:05.....	3.158×10^5	RTT150	R_C	2700.0	21.18 ± 0.04	3
Aug 24 08:46:32.....	3.535×10^5	P60	R_C	8400.0	21.22 ± 0.11	1
Aug 25 09:33:11.....	4.427×10^5	P60	R_C	2880.0	21.34 ± 0.13	1
Aug 26 05:05:39.....	5.130×10^5	HET	R_C	600.0	21.57 ± 0.08	1
Aug 26 08:28:20.....	5.252×10^5	P60	R_C	3600.0	21.64 ± 0.12	1
Aug 27 08:37:13.....	6.121×10^5	P60	R_C	4800.0	21.80 ± 0.12	1
Aug 27 22:49:53.....	6.633×10^5	RTT150	R_C	1500.0	22.02 ± 0.10	5
Sep 26 01:39:38.....	3.179×10^6	<i>HST</i>	F625W	800.0	24.59 ± 0.08	1
.....	R_C	...	24.55 ± 0.08	1
Aug 20 06:40:21.....	328.0	P60	I_C	60.0	14.91 ± 0.02	1
Aug 20 06:45:19.....	626.0	P60	I_C	60.0	14.42 ± 0.01	1
Aug 20 06:50:06.....	913.0	P60	I_C	60.0	14.78 ± 0.01	1

TABLE 5—Continued

Mean Observation Date (2005 UT)	t_{BAT} (s)	Telescope	Filter	Exposure Time (s)	Magnitude ^a (Vega)	Reference
Aug 20 06:56:37.....	1.304×10^3	P60	I_C	120.0	15.24 ± 0.02	1
Aug 20 07:07:15.....	1.942×10^3	P60	I_C	120.0	15.74 ± 0.02	1
Aug 20 07:18:03.....	2.590×10^3	P60	I_C	120.0	16.07 ± 0.02	1
Aug 20 07:40:11.....	3.918×10^3	P60	I_C	360.0	16.54 ± 0.03	1
Aug 20 08:21:15.....	6.382×10^3	P60	I_C	360.0	17.02 ± 0.05	1
Aug 20 08:46:26.....	7.893×10^3	P60	I_C	360.0	17.22 ± 0.04	1
Aug 20 08:46:53.....	7.920×10^3	PROMPT-3	I_C	1560.0	17.31 ± 0.08	4
Aug 20 09:11:47.....	9.414×10^3	P60	I_C	360.0	17.23 ± 0.05	1
Aug 20 09:37:27.....	1.095×10^4	P60	I_C	360.0	17.34 ± 0.03	1
Aug 20 10:21:01.....	1.357×10^4	P60	I_C	360.0	17.48 ± 0.04	1
Aug 20 10:47:55.....	1.518×10^4	P60	I_C	360.0	17.68 ± 0.04	1
Aug 20 11:14:54.....	1.680×10^4	P60	I_C	360.0	17.71 ± 0.05	1
Aug 20 11:42:22.....	1.845×10^4	P60	I_C	360.0	17.72 ± 0.04	1
Aug 21 04:04:53.....	7.740×10^4	PROMPT-3	I_C	5440.0	18.33 ± 0.11	4
Aug 22 00:07:53.....	1.496×10^5	RTT150	I_C	1800.0	19.74 ± 0.07	2
Aug 22 07:25:05.....	1.758×10^5	P60	I_C	6840.0	19.97 ± 0.12	1
Aug 22 23:06:41.....	2.323×10^5	RTT150	I_C	3900.0	20.37 ± 0.05	3
Aug 23 08:22:42.....	2.657×10^5	P60	I_C	7560.0	20.48 ± 0.12	1
Aug 23 22:24:05.....	3.162×10^5	RTT150	I_C	2700.0	20.78 ± 0.09	3
Aug 24 09:11:48.....	3.550×10^5	P60	I_C	8400.0	20.59 ± 0.11	1
Aug 25 10:44:39.....	4.470×10^5	P60	I_C	2400.0	21.02 ± 0.15	1
Aug 26 04:49:33.....	5.121×10^5	HET	I_C	1200.0	21.25 ± 0.10	1
Aug 26 09:27:24.....	5.288×10^5	P60	I_C	4800.0	21.17 ± 0.14	1
Aug 27 08:34:02.....	6.120×10^5	P60	I_C	4440.0	21.30 ± 0.13	1
Sep 26 02:01:58.....	3.180×10^6	HST	F775W	800.0	24.32 ± 0.09	1
	I_C	...	24.27 ± 0.09	1
Aug 20 06:41:50.....	417.0	P60	z'	60.0	13.93 ± 0.11	1
Aug 20 06:46:45.....	712.0	P60	z'	60.0	14.27 ± 0.14	1
Aug 20 06:51:50.....	1.017×10^3	P60	z'	60.0	14.62 ± 0.21	1
Aug 20 06:59:16.....	1.463×10^3	P60	z'	120.0	15.02 ± 0.13	1
Aug 20 07:09:56.....	2.103×10^3	P60	z'	120.0	15.49 ± 0.14	1
Aug 20 07:20:45.....	2.752×10^3	P60	z'	120.0	15.96 ± 0.20	1
Sep 26 03:06:14.....	3.184×10^6	HST	F850LP	1600.0	24.09 ± 0.09	1

^a Errors quoted are 1 σ photometric and instrumental errors summed in quadrature. Galactic extinction [$E(B - V) = 0.044$; Schlegel et al. 1998] has been incorporated in the reported magnitudes.

REFERENCES.—(1) This paper; (2) Bikmaev et al. 2005; (3) Khamitov et al. 2005; (4) MacLeod & Nysewander 2005; (5) Aslan et al. 2005.

TABLE 6
RADIO OBSERVATIONS OF GRB 050820A

Observation Date (2005 UT)	t_{BAT} (days)	Frequency (GHz)	Flux Density ^a (μJy)
Aug 20.39.....	0.116	4.86	<102
Aug 20.39.....	0.116	8.46	110 ± 40
Aug 20.39.....	0.116	22.5	<186
Aug 21.20.....	0.93	8.46	634 ± 62
Aug 22.42.....	2.15	4.86	256 ± 78
Aug 22.42.....	2.15	8.46	419 ± 50
Aug 22.42.....	2.15	22.5	<216
Aug 24.38.....	4.11	4.86	171 ± 47
Aug 24.38.....	4.11	8.46	74 ± 36
Aug 25.32.....	5.05	8.46	<114
Aug 26.40.....	6.13	8.46	<120
Aug 28.37.....	8.10	8.46	166 ± 45
Sep 1.33.....	12.06	8.46	89 ± 39
Sep 4.18.....	14.91	8.46	106 ± 33
Sep 15.20.....	25.93	8.46	76 ± 30
Oct 20.19.....	60.92	8.46	<70

^a Errors quoted for detections are at the 1 σ level. Upper limits are reported as 2 σ rms noise.

We have divided the X-ray and optical light curves into segments (phases 1–4) based on noticeable temporal breaks. We then investigated each segment independently, fitting the light curve and spectra to power-law decay indices of the form $F_\nu \propto t^{-\alpha} \nu^{-\beta}$. The lack of a bright afterglow makes such analysis impossible in the radio.

The X-ray and optical light curves, with temporal divisions marked by dashed vertical lines, are shown in Figure 4. Phase 1 begins with the BAT trigger and ends with the resumption of X-ray observations at $t_{\text{break},1} \equiv 4785$ s. The X-ray and optical data behave differently in phase 1, resulting in unique subdivisions for the two bandpasses. However, phase 1 is the only epoch to show such divergent behavior.

With the emergence of *Swift* from the SAA at $t_{\text{break},1}$, both the X-ray and optical light curves exhibit a relatively shallow decline. This characterizes phase 2, which ends when the X-ray decline steepens at $t_{\text{break},2} \equiv 8.7 \times 10^4$ s. The decay slope in phase 3 is steeper than in phase 2 in both bandpasses.

Phase 3 extends out to the last X-ray detection at $t_{\text{break},3} \equiv 1.7 \times 10^6$ s. Between this time and the *HST* optical observations, the optical decay must have significantly steepened. This last epoch, with only optical data, we define as phase 4.

The results of this power-law analysis are shown in Tables 4 and 7. Each bandpass is discussed in further detail below.

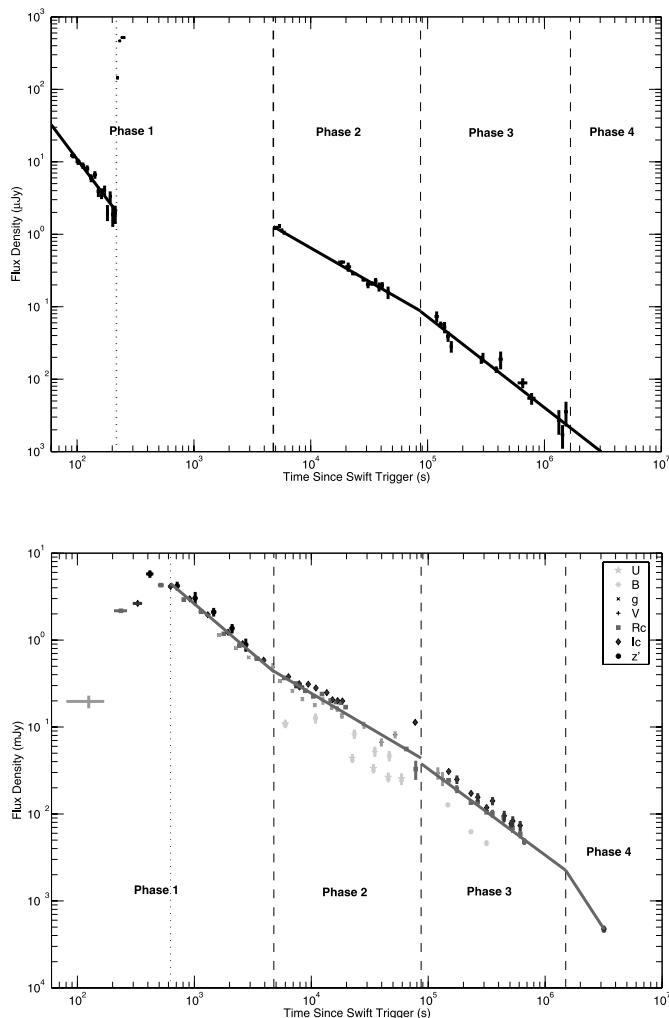


FIG. 4.—X-ray (*top*) and optical (*bottom*) light curves of GRB 050820A. Both bandpasses have been divided into four segments (phases 1–4), each shown with a vertical dashed line. The unique subdivision of phase 1 is shown as a dotted line in both plots. *Top*: 2–10 keV X-ray fluxes were converted to flux densities at 5 keV using the average spectral slope for each phase. It was assumed the spectrum remained constant from phase 2 to phase 3. The best-fit X-ray temporal decay is shown with a solid line. *Bottom*: Magnitudes were converted to flux densities using zero points from Fukugita et al. (1995). The best-fit R_C band temporal decay is shown with a solid line. For full details of our analysis, see § 3 and Tables 4 and 7.

3.1. X-Ray Light Curve and Spectrum

The X-ray light curve of GRB 050820A is shown in the top panel of Figure 4. In phase 1, we see two distinct behaviors: Initially the X-ray light curve falls rapidly with a decay slope $\alpha_{1a,X} = 2.2 \pm 0.3$. This continues until $t_{\text{BAT}} = 217$ s, and we define this as phase 1a_X. The X-ray emission then rises rapidly ($217 \text{ s} < t_{\text{BAT}} < 257$ s; phase 1b_X), after which *Swift* enters the SAA. It is clear from the correlation between the γ -ray and X-ray emission in this epoch that the two are related (see Fig. 1c). A full study of the properties of phase 1b_X is left to § 4.2.

Following *Swift*'s emergence from the SAA, the light curve in phase 2 shows evidence for a shallower epoch of decline. With the large gap in coverage, we cannot constrain when this transition occurs. We therefore define $t_{\text{break},1}$ to coincide with the resumption of XRT observations at $t_{\text{BAT}} = 4785$ s. A similar break in the optical light curve is also seen near this time (§ 3.2).

The X-ray data after $t_{\text{break},1}$ are not well fitted by a single power-law decay ($\chi_r^2 = 3.7$; 31 dof), due mostly to a steepening of

TABLE 7
OPTICAL AFTERGLOW SPECTRAL AND TEMPORAL FITS

Phase	$t_{\text{BAT}}^{\text{start}}$ (s)	$t_{\text{BAT}}^{\text{stop}}$ (s)	α	β	χ_r^2/dof
1a.....	T_{BAT}	626	-0.35 ± 0.02	...	3.00/13
1b.....	626	4.8×10^3	0.97 ± 0.01	0.57 ± 0.06	1.53/14
2.....	4.8×10^3	8.7×10^4	0.78 ± 0.01	0.77 ± 0.08	5.7/31
3.....	8.7×10^4	1.7×10^6	0.99 ± 0.06	...	1.43/18
4.....	1.7×10^6	3.2×10^6	≥ 2.1

NOTES.—We have fitted the optical data to a power-law model of the form $F_\nu \propto t^{-\alpha} \nu^{-\beta}$ where possible. In some phases (1a and 3), we have limited spectral coverage and could not meaningfully constrain β . Thus, we have only fitted for the temporal decay index α . In phase 4, we can only place an upper limit on the decay slope. All errors quoted are 90% confidence limits.

the decay at $t_{\text{BAT}} \approx 10^5$ s. Fitting a broken power-law model to this data, we find an acceptable fit with $t_{\text{break},2} = (8.7 \pm 2.4) \times 10^4$ s ($\chi_r^2 = 1.19$, 25 dof). The resulting decay index before the break (phase 2) is $\alpha_{2,X} = 0.93 \pm 0.03$. For phase 3, we find $\alpha_{3,X} = 1.25 \pm 0.07$.

The X-ray spectral index in phase 1a_X is relatively steep: $\beta_{1a,X} = 0.90 \pm 0.09$. The spectrum hardens significantly in phase 1b_X ($\beta_{1b,X} = -0.10 \pm 0.03$), further justifying our decision to split phase 1 into two separate X-ray segments. In phase 2, the spectrum softens again, to $\beta_{2,X} = 1.20 \pm 0.04$. There are too few X-ray counts in phase 3 to meaningfully constrain the spectrum.

The results of our analysis of the X-ray data set are summarized in Table 4.

3.2. Optical Light Curve and Spectrum

The optical light curve from GRB 050820A is shown in the bottom panel of Figure 4. Phases 1 ($0 \text{ s} < t_{\text{BAT}} < 4785$ s), 2 ($4785 \text{ s} < t_{\text{BAT}} < 8.7 \times 10^4$ s), and 3 ($8.7 \times 10^4 \text{ s} < t_{\text{BAT}} < 1.7 \times 10^6$ s) of the optical light curve have already been defined in terms of the X-ray decay. However, unlike the X-ray, the earliest optical observations indicate that the afterglow was getting brighter with time (Cenko & Fox 2005; Wren et al. 2005). This rise continues until a peak at $t_{\text{BAT}} \approx 600$ s, marking the end of phase 1a_{opt}. After the peak, the optical light curve in all four P60 filters decays steadily with $\alpha_{1b,\text{opt}} = 0.97 \pm 0.01$ until $t_{\text{break},1}$. We note that for this and all subsequent phases, we have constrained α to be identical in all optical filters. A more thorough discussion of phase 1 is left to § 4.2.

Much like the X-ray, the optical decay in phases 2 and 3 is poorly fitted by a single power law ($\chi_r^2 = 13.7$, 49 dof). In phase 2, the optical decay noticeably flattens ($\alpha_{2,\text{opt}} = 0.78 \pm 0.01$). A much higher degree of variability is seen in the different filters, resulting in a poor fit statistic. After $t_{\text{break},2}$ the decay in phase 3 is again steeper and more uniform, with $\alpha_{3,\text{opt}} = 0.99 \pm 0.06$.

It is clear that if we extrapolate the decay from phase 3 out to the *HST* observations, the late-time flux is greatly overestimated. We conclude therefore that a break has occurred in the light curve sometime after $t_{\text{break},3}$, and thus we define phase 4 to span $1.7 \times 10^6 \text{ s} < t_{\text{BAT}} < 3.2 \times 10^6$ s. We estimate the temporal decay in phase 4 to be $\alpha_{4,\text{opt}} \geq 2.1$.

Due to the limited spectral coverage of our observations, we are unable to provide meaningful constraints on the spectral index β in phases 1a_{opt}, 3, and 4. For the remaining epochs, we have excluded the *U*- and *B*-band data from our spectral fits, as these are expected to lie below the Ly α absorption edge at this redshift. We attempted to solve for the host galaxy reddening [$A_V(\text{host})$] using extinction laws for the Milky Way and the Large and Small

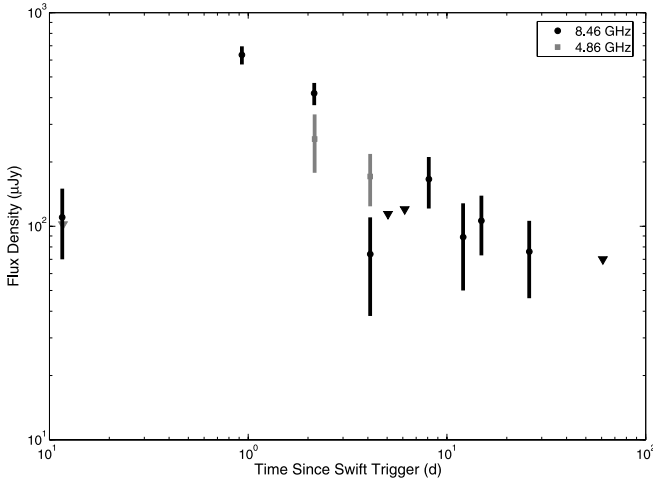


FIG. 5.—Radio afterglow of GRB 050820a. The early rise in the radio light curve at $t_{\text{BAT}} \approx 1$ day is most easily understood as a reverse shock caused by late-time energy injection, as seen in both the optical and X-ray light curves. The most striking feature of the radio light curve, however, is the lack of a bright radio afterglow at late times (see § 4.4).

Magellanic Clouds from Pei (1992). In all cases, we find a host extinction consistent with zero. While this result is inconsistent with the column density derived from high-resolution spectroscopy (Ledoux et al. 2005), it is in agreement with the low host extinction values seen in almost all well-sampled pre-*Swift* afterglows (Kann et al. 2006).

Ignoring host reddening, we find $\beta_{1\text{b,opt}} = 0.57 \pm 0.06$ and $\beta_{2\text{,opt}} = 0.77 \pm 0.08$. While the optical spectrum appears to have steepened in phase 3, the poor fit quality of this phase precludes any firm conclusions from being drawn.

The results of our analysis of the optical data set are shown in Table 7.

3.3. Radio Light Curve

The radio emission rises to a peak sometime around 1 day after the burst (see Fig. 5 and Table 6). The radio spectrum at early times is quite chaotic, transitioning through a peak around 8.5 GHz at $t_{\text{BAT}} = 2.15$ days to optically thin 4.11 days after the burst. We note that some of the variation at early times may be due to interstellar scintillation (Goodman 1997) as has been seen in many other radio afterglows (see, e.g., Frail et al. 1997).

The late-time ($t > 7$ days) radio data show no sign of any afterglow brighter than $200 \mu\text{Jy}$. This is in marked contrast to the bright optical and X-ray afterglows and is one of the most difficult aspects of the afterglow to account for (§ 4.4).

4. DISCUSSION

In this section we use the results from our previous analysis to try to explain the broadband emission from GRB 050820A in the context of the standard fireball model (for a review see, e.g., Piran 2005). In this model, highly relativistic ejecta are emitted by a central engine as shells with varying Lorentz factors. Shock fronts formed between these shells produce the high-energy prompt emission; these collisions are known as internal shocks. Emission from internal shocks is highly nonthermal and results in an (empirically determined) power-law spectrum with a cutoff exponential: $dN/dE \propto E^\alpha e^{-E/E_0}$ (Band et al. 1993). As the relativistic shells expand and slow down, they eventually encounter the circumburst medium. Again a collisionless shock front forms, accelerating electrons to a power-law distribution of Lorentz factors with ex-

ponent p and minimum Lorentz factor γ_m . It is assumed that a constant fraction of the total energy density is partitioned to the electrons (ϵ_e) and the magnetic field (ϵ_B). These accelerated electrons then emit synchrotron radiation, powering the long-lived X-ray, optical, and radio afterglow (the forward, external shock). Additional emission can be generated from shock heating of the ejecta (the reverse shock), leading to a rapidly decaying flare in the optical and radio light curve (Sari & Piran 1999b).

The observed afterglow spectrum depends on the relative ordering of the three critical frequencies: ν_a , the frequency where self-absorption becomes important, ν_m , the characteristic frequency of the emission, and ν_c , the frequency above which electrons are able to cool efficiently through radiation. Typical afterglow observations occur when $\nu_a < \nu_m < \nu_c$ (i.e., slow cooling), resulting in the following spectral indices (Sari et al. 1998):

$$F_\nu \propto \begin{cases} \nu^2, & \nu < \nu_a, \\ \nu^{1/3}, & \nu_a < \nu < \nu_m, \\ \nu^{-(p-1)/2}, & \nu_m < \nu < \nu_c, \\ \nu^{-p/2}, & \nu > \nu_c. \end{cases} \quad (1)$$

The light curve produced by such emission depends on the radial profile of the circumburst medium into which the shock is expanding. The simplest circumburst medium to consider is one in which the density is constant ($\rho \propto r^0$). This scenario is also referred to as an interstellar medium (ISM). In this case, the flux density will scale as (Sari et al. 1998)

$$F_\nu \propto \begin{cases} t^{1/2}, & \nu < \nu_a, \\ t^{1/2}, & \nu_a < \nu < \nu_m, \\ t^{3(1-p)/4}, & \nu_m < \nu < \nu_c, \\ t^{(2-3p)/4}, & \nu > \nu_c. \end{cases} \quad (2)$$

Alternatively, if we eliminate p from the above equations, we find a characteristic relation between α and β in each spectral regime known as a ‘‘closure relation’’ (Price et al. 2002):

$$\alpha = \begin{cases} \frac{\beta}{4}, & \nu < \nu_a, \\ \frac{3\beta}{2}, & \nu_a < \nu < \nu_m, \\ \frac{3\beta}{2}, & \nu_m < \nu < \nu_c, \\ \frac{3\beta - 1}{2}, & \nu > \nu_c. \end{cases} \quad (3)$$

The long-soft class of GRBs, however, is thought to arise from the deaths of massive stars, as they collapse to form black holes: the so-called collapsar model (Woosley 1993). In the late stages of evolution, massive Wolf-Rayet stars are stripped of their outer envelopes in a wind, leaving behind a signature $\rho \propto r^{-2}$ density profile that should be discernible in the afterglow light curve. The analogous temporal decay indices for a windlike medium are (Chevalier & Li 2000)

$$F_\nu \propto \begin{cases} t^1, & \nu < \nu_a, \\ t^0, & \nu_a < \nu < \nu_m, \\ t^{(1-3p)/4}, & \nu_m < \nu < \nu_c, \\ t^{(2-3p)/4}, & \nu > \nu_c. \end{cases} \quad (4)$$

The derived closure relations are

$$\alpha = \begin{cases} \frac{\beta}{2}, & \nu < \nu_a, \\ \frac{3\beta + 1}{2}, & \nu_a < \nu < \nu_m, \\ \frac{3\beta + 1}{2}, & \nu_m < \nu < \nu_c, \\ \frac{3\beta - 1}{2}, & \nu > \nu_c. \end{cases} \quad (5)$$

The above temporal decay indices and closure relations (eqs. [2]–[5]) are only valid for spherically symmetric emission. GRBs, however, are thought to be beamed events. At early times, observers only notice emission from a narrow cone (opening angle $\theta \sim \Gamma^{-1}$, where Γ is the Lorentz factor of the expanding shock) due to relativistic beaming (see, e.g., Rybicki & Lightman 1979). As the shock slows, however, lateral spreading of the jet becomes important, and the observer eventually notices “missing” emission from wider angles (Rhoads 1999; Sari et al. 1999). This hydrodynamic transition manifests itself as an achromatic steepening in the afterglow light curve, with an expected post-jet break decay proportional to t^{-p} .

With the above formulation in hand, we now wish to understand the physical implications of our previous analysis.

4.1. Early γ -Ray Emission

The most striking feature of the γ -ray light curve of GRB 050820A is the large gap between the initial pulse that triggered the *Swift* BAT (peak A in Fig. 1b) and the bulk of the high-energy emission ($t_{\text{BAT}} > 200$ s). The natural question arises as to whether this “precursor”²¹ results from the same physical mechanism as the bulk of the high-energy emission. Many models predict a high-energy component distinct from the prompt GRB at early times. Possible mechanisms include the transition from an optically thick to an optically thin environment in the fireball itself (Paczynski 1986; Lyutikov & Usov 2000; Mészáros & Rees 2000; Lyutikov & Blandford 2003), or the interaction of a jet with a progenitor, presumably a collapsing Wolf-Rayet star (Ramirez-Ruiz et al. 2002; Waxman & Mészáros 2003).

We can securely rule out both of these models for the precursor of GRB 050820A, as both predict a thermal spectrum. Fitting a thermal model to the BAT precursor spectrum results in a fit statistic of $\chi_r^2 = 3.4$ (75 dof), while a nonthermal power-law model provides an excellent fit ($\chi_r^2 = 1.07$, 75 dof).

While the precursor may be nonthermal, it is noticeably softer than the majority of the remaining prompt emission (see Fig. 2, *bottom two panels*). A search for precursors in a sample of long, bright BATSE bursts revealed such a soft, nonthermal component in a sizable fraction (20%–25%) of these events (Lazzati 2005). Furthermore, two of the longest, brightest *Swift* bursts observed to date, GRB 041219A (Vestrand et al. 2005; McBreen et al. 2006) and GRB 060124 (Romano et al. 2006), show a faint, soft precursor followed by a large time lag (570 s in the case of GRB 060124).

These soft precursors are inconsistent with the main prompt emission in most GRBs, which exhibits a hard-to-soft evolution in the γ -ray spectrum (Ford et al. 1995; Frontera et al. 2000). The γ -ray light curve of GRB 050820A conforms to this trend only if

²¹ Here we define a precursor as an event that is well separated from and contains only a small fraction of the total high-energy emission. Unlike some other authors, our definition is independent of the mechanism behind the emission. Peak A in GRB 050820A is then clearly a precursor.

we ignore the precursor. Furthermore, it is difficult to conceive of a scenario by which internal shocks can generate such long periods of quiescence in a sustained outflow. The large time lag, soft nature, and repeated occurrence of these precursors hint that they are in fact due to a different emission mechanism than the internal dissipation thought to power the bulk of the high-energy emission. However, we cannot state this conclusively, as would be the case if the precursors were thermal.

If we assume a different emission mechanism, the prompt emission did not begin until 222 s after the *Swift* trigger. This seemingly small discrepancy in defining T_0 affects the calculated temporal decay indices, particularly during the early afterglow (§ 4.4). For all temporal decay indices calculated in this work, we consider T_0 to coincide with the beginning of the bulk of the high-energy emission (i.e., 06:38:35 UT on 2005 August 20).

Finally, we consider the early X-ray emission. The temporal decay slope at early times ($\alpha_{1a,X} = 2.2$) is too steep to be attributed to a standard forward shock afterglow. The most popular explanation for the rapid decline of early X-ray emission in *Swift* GRBs is “high-latitude emission,” i.e., prompt emission from large angles ($\theta > \Gamma^{-1}$) that, due to relativistic beaming effects, reaches the observer at late times [$\Delta t \sim (1+z)R\theta^2/2c$; Kumar & Panaitescu 2000]. However, this results in a well-defined relationship between the spectral and temporal indices ($\alpha = \beta + 2$) that is inconsistent with the observed values for GRB 050820A.

Zhang et al. (2006) discuss possible mechanisms that could cause the early-time decay slope to deviate from this behavior. The most realistic possibility is if the X-rays were below the cooling frequency at this very early epoch. Then the closure relation would take the form $\alpha \approx 1 + 3\beta/2 = 2.4$ (Sari & Piran 1999a), in good agreement with the observed value.

4.2. Contemporaneous X-Ray and Optical Emission

Given the long duration and bright fluence, GRB 050820A provides a rare opportunity to study contemporaneous emission in the optical, X-ray, and γ -ray bandpasses. In Figure 1 we show the early-time ($t_{\text{BAT}} \lesssim 800$ s) emission in X-rays (Fig. 1c) and optical (Fig. 1d) overlaid onto the high-energy light curve of GRB 050820A.

A look at the X-ray data in Figure 1c shows a strong correlation between the X-ray and γ -ray light curves. The X-ray light curve, previously in the midst of a decline, abruptly jumps in sync with the high-energy emission at $t_{\text{BAT}} \approx 222$ s (phase 1b_X). In addition to temporal similarities, the X-ray photon index at this epoch ($\Gamma_{\text{XRT}} = 0.90 \pm 0.03$) is much harder than at any other epoch in the X-ray light curve and similar to that derived from the BAT ($\Gamma_{\text{BAT}} = 1.07 \pm 0.06$). Thus motivated, we have performed a joint fit of the BAT and XRT spectra at this epoch. Unfortunately, *Konus-Wind* had yet to trigger, and so no high-energy multichannel spectra are available from that instrument. We find that both bandpasses are well fitted by a single power law with index $\Gamma = 0.94 \pm 0.03$ ($\chi_r^2 = 1.3$, 391 dof). The resulting unfolded spectrum is shown in Figure 6. We conclude that the X-rays in phase 1b_X are generated by the same mechanism as the prompt emission.

It is clear from Figure 1d that, unlike in the X-ray band, there is no strong correlation between optical and γ -ray flux from GRB 050820A. Radical spectral evolution would be required in the optical to explain both bandpasses as arising from the same emission mechanism. We consider this scenario highly unlikely and conclude that, at the very least, the dominant contribution to the optical emission in phase 1 has a different origin than the prompt emission.

We next consider if our optical observations in phase 1 can be explained solely in terms of the standard afterglow formulation. We have attempted to fit both a simple broken power law (Sari

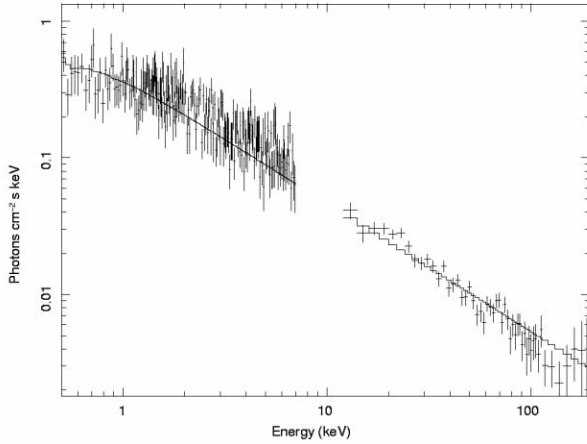


FIG. 6.—Joint BAT/XRT spectrum of the main pulse of prompt emission ($217 \text{ s} < t_{\text{BAT}} < 257 \text{ s}$). While there is no region of direct overlap, the XRT data are clearly the low-energy tail of the prompt BAT emission, forming one continuous spectrum. The best-fit spectrum ($\Gamma = 0.94$) is shown as a solid line. Both the BAT and XRT data have been binned for plotting purposes.

et al. 1998) and an analytic solution for the flux density near the optical peak (Granot & Sari 2002) to our R_C , I_C , and z' band early-time data. The resulting fit quality is quite poor ($\chi_r^2 = 3.0$, 14 dof), with the dominant contribution coming from the data in phase 1a_{opt} (i.e., before the peak). In spite of the poor fit, we have included the results for phase 1a_{opt} in Table 7 for reference.

This result is not unexpected, as Vestrand et al. (2006) have shown that contemporaneous optical imaging of GRB 050820A with the RAPTOR telescope can be well fitted as the sum of two independent components: one representing the forward shock and another proportional to the high-energy prompt emission. We attempted an analogous fit with the P60 and *Konus-Wind* data set. While a better fit statistic ensues, we still do not find an acceptable result ($\chi_r^2 = 2.2$, 14 dof). We conclude that the relatively sparse time sampling of our observations, coupled with the frequent filter changes, makes it impossible to verify this result.

Independent of any correlation between the prompt optical and γ -ray emission, we note that the decay after $t_{\text{BAT}} = 600 \text{ s}$ is dominated by the forward shock. Unlike the bright, early-time emission seen from GRB 990123 (Akerlof et al. 1999), we see

no evidence for rapidly decaying [$\alpha_{\text{RS}} = (27p + 7)/35 \approx 2$; Kobayashi 2000] reverse shock emission from an optical flare.

Finally, using the combination of optical and γ -ray data, we consider the broadband SED of GRB 050820A at early times. For each of the contemporaneous optical observations, we have extracted fluxes and (where possible) spectra from the corresponding *Konus-Wind* observations (Fig. 7 and Table 8). Following the method of Vestrand et al. (2005), we have calculated the γ -ray-to-optical color index, $C_{O\gamma} \equiv -2.5 \log [F(\text{opt})/F(\gamma)]$, or lower limits, for each interval. The ratio varies significantly over the course of our observations. The value of $C_{O\gamma} = 12.5$ in interval 2 is consistent with that seen from GRB 041219a, while later intervals are even brighter in the optical. In fact, the optical-to- γ -ray flux ratio in interval 5 is over 240 times larger than that observed for GRB 050401 (Rykoff et al. 2005). Evidently a large diversity exists in the broadband SEDs of GRBs at early times.

4.3. Late-Time Energy Injection

The majority of XRT light curves observed to date have exhibited a period of shallow decline ($0.2 \lesssim \alpha \lesssim 0.8$) that is inconsistent with the standard afterglow formulation (Nousek et al. 2006). Two models have been invoked to explain this phase, both of which involve injecting energy into the forward shock at late times ($t \gg t_{\text{GRB}}$; for a review see, e.g., Zhang et al. 2006). In the first, the central engine is active for long time periods, $t \gg t_{\text{GRB}}$. The late-time emission of highly relativistic material injects additional energy into the forward shock, flattening the decay slope (Katz & Piran 1997; Rees & Mészáros 2000). Alternatively, toward the end of the γ -ray emission, the central engine may inject material with a smooth distribution of (decreasing) Lorentz factors. Slower moving material will catch up with the forward shock when it has swept up enough circumburst material, resulting in a smooth injection of energy at late times (Rees & Mészáros 1998; Sari & Mészáros 2000). While both models explain the flattening of the XRT light curves, they provide different constraints on the nature of the central engine.

In the first (long-lived central engine) model, the central engine's luminosity, $L(t)$, is characterized as

$$L(t) = L_0(t/t_0)^{-q}. \quad (6)$$

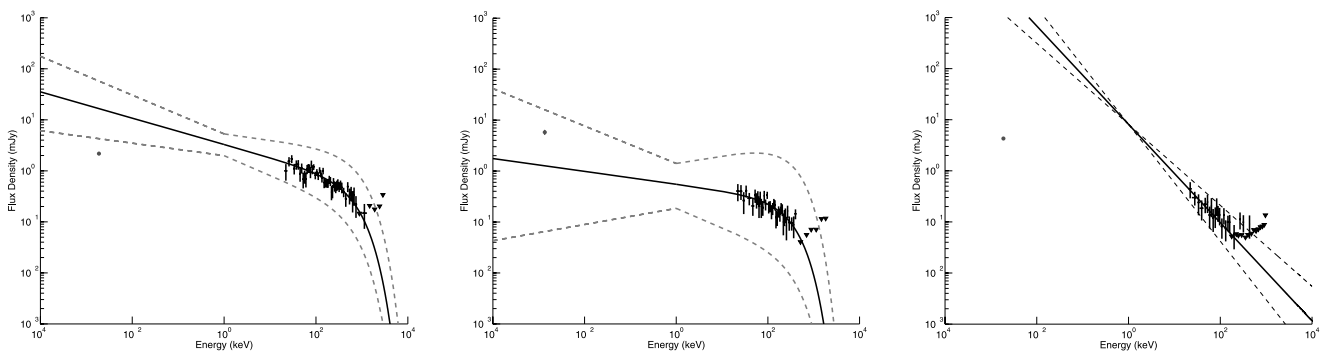


FIG. 7.—Early-time broadband SED of GRB 050820a. *Konus-Wind* spectral data for the given intervals (see Table 8 for definitions of the intervals) are shown (crosses) alongside the corresponding optical observations (circles). The 2σ upper limits in the high-energy spectra are plotted as triangles. The best-fit model to the *Konus-Wind* spectrum is shown as a solid line, and the dashed lines show the 90% confidence intervals for the spectral fits. The ratio of optical to γ -ray flux varies significantly between the three intervals. *Left*: Interval 2. This interval covers only a small fraction of the time of the corresponding P60 image because *Konus-Wind* only triggered on GRB 050820a (and hence began collecting multichannel spectra) in the middle of this image. The optical R_C band data point lies below the extrapolation of the γ -ray spectrum. *Middle*: Interval 4. Here the *Konus-Wind* and P60 intervals are nearly simultaneous. Unlike the other intervals, the P60 z' band point lies above the predicted value and within the 90% confidence interval of the extrapolation of the high-energy spectrum. *Right*: Interval 5. Here the high-energy extrapolation greatly overestimates the optical flux. However, the γ -ray flux in this interval is quite low, and in particular the low number of high-energy photons makes it difficult to constrain a cutoff power-law spectrum. In fact, this interval was best fitted with a simple power-law spectrum.

TABLE 8
JOINT γ -RAY/OPTICAL EARLY-TIME DATA

Interval ID	$t_{\text{BAT}}^{\text{start}}$ (s)	Duration (s)	γ -Ray Flux ^a (10^{-8} ergs cm^{-2} s^{-1})	α^b	E_p^b (keV)	χ^2/dof	Optical Filter	Optical Flux Density ^a (mJy)	$C_{O\gamma}^c$
1.....	80.949	85.376	<1.3	V	0.20 ± 0.03	<10.2
2.....	257.839	8.448	$96.2^{+0.8}_{-13.9}$	1.26 ± 0.14	510^{+211}_{-120}	0.83/62	R_C	2.17 ± 0.08	12.4
3.....	297.775	59.904	<3.2	I_C	2.64 ± 0.04	<8.8
4.....	389.167	57.344	$19.06^{+0.03}_{-6.61}$	$1.13^{+0.24}_{-0.29}$	269^{+107}_{-59}	0.78/62	z'	5.77 ± 0.57	10.0
5.....	487.471	57.344	$9.35^{+0.53}_{-2.38}$	1.96 ± 0.18	...	1.01/58	R_C	4.28 ± 0.08	9.2
6.....	602.159	49.152	<2.3	I_C	4.14 ± 0.05	<7.9
7.....	684.079	57.344	<4.1	z'	4.20 ± 0.49	<8.7

^a Errors quoted are at the 1σ level.

^b Spectral fits of the form $dN/dE \propto E^{-\alpha} \exp^{-(2-\alpha)E/E_p}$ were performed for the case of intervals 2 and 4. For interval 5, the highest energy data were not of sufficient quality to estimate E_p . Instead, a power-law fit ($dN/dE \propto E^{-\alpha}$) was used. Errors quoted are 90% confidence limits.

^c The γ -ray-to-optical color index: $C_{O\gamma} \equiv -2.5 \log [F(\text{opt})/F(\gamma)]$.

This results in the following spectral and temporal power-law indices for a constant-density medium:

$$\alpha = \begin{cases} \frac{5q-8}{6} = (q-1) + \frac{(2+q)\beta}{2}, & \nu < \nu_m, \\ \frac{(2p-6)+(p+3)q}{4} = (q-1) + \frac{(2+q)\beta}{2}, & \nu_m < \nu < \nu_c, \\ \frac{(2p-4)+(p+2)q}{4} = \frac{q-2}{2} + \frac{(2+q)\beta}{2}, & \nu > \nu_c. \end{cases} \quad (7)$$

For a windlike medium, the analogous results are

$$\alpha = \begin{cases} \frac{q-1}{3} = \frac{q}{2} + \frac{(2+q)\beta}{2}, & \nu < \nu_m, \\ \frac{(2p-2)+(p+1)q}{4} = \frac{q}{2} + \frac{(2+q)\beta}{2}, & \nu_m < \nu < \nu_c, \\ \frac{(2p-4)+(p+2)q}{4} = \frac{q-2}{2} + \frac{(2+q)\beta}{2}, & \nu > \nu_c. \end{cases} \quad (8)$$

The refreshed shock scenario is parameterized in terms of the amount of mass ejected with Lorentz factor greater than γ :

$$M(>\gamma) \propto \gamma^{-s}. \quad (9)$$

For the circumburst profiles considered here, we can define a new variable, \hat{q} , such that we reproduce identical afterglow behavior to that of equation (7) or equation (8) by simply substituting \hat{q} for q . Parameter \hat{q} is related to the mass ejection parameter s by the following equations (Zhang et al. 2006):

$$\hat{q} = \begin{cases} \frac{10-2s}{7+s}, & \text{ISM}, \\ \frac{4}{3+s}, & \text{wind}. \end{cases} \quad (10)$$

While the X-ray decay in phase 2 is not as flat as that seen in other *Swift* bursts, the temporal and spectral decay indices are nonetheless inconsistent with the standard afterglow model for $\nu(X) > \nu_c$ (last line of eqs. [3] and [5]). Furthermore, the optical light curve shows a flattening during phase 2 and is inconsistent with the closure relations in either medium for $\nu_m < \nu(\text{opt}) < \nu_c$ (third line of eqs. [3] and [5]). We conclude that we

are therefore seeing a milder version of the energy injection phase present in many *Swift* XRT afterglows.

For the X-ray data in phase 2, we find an acceptable fit for the energy injection models only if $\nu(X) > \nu_c$. This corresponds to values of $q_X = 0.66 \pm 0.08$ ($s_{X,\text{ISM}} = 2.0 \pm 0.3$, $s_{X,\text{wind}} = 3.1 \pm 0.7$) and $p_X = 2.4 \pm 0.2$. The optical data in phase 2 are best fitted with a constant-density medium and $\nu_m < \nu(\text{opt}) < \nu_c$: $q_{\text{opt}} = 0.73 \pm 0.09$ ($s_{\text{ISM,opt}} = 1.8 \pm 0.3$) and $p_{\text{opt}} = 2.5 \pm 0.2$. Both the X-ray and the optical fall in the spectral regime we would expect, providing further confidence in this interpretation.

A prediction of the energy injection hypothesis is a bright reverse shock at early times most easily visible in the radio (Sari & Mészáros 2000). A reverse shock nicely explains the rapid decline in flux at 8.5 GHz from 1 to 4 days after the burst. Furthermore, the transition from a spectrum peaked around 8.5 GHz at $t_{\text{BAT}} = 2.15$ days to an optically thin radio spectrum at $t_{\text{BAT}} = 4.11$ days can be understood as the reverse shock peak frequency, ν_m^{RS} , passing through the radio. Since $\nu_m^{\text{RS}} \approx \nu_m^{\text{FS}}/\gamma^2$, this should occur well before the forward shock peak frequency reaches the radio bands.

Distinguishing between the two theories to explain the energy injection is quite difficult, as both models can be identically parameterized. Progress in this area would require a large sample of bursts with detailed contemporaneous X-ray and optical light curves. If the refreshed shocks are due to continued engine activity, they should be correlated with the bright X-ray flares seen in some XRT afterglows. On the other hand, if the flat decay is caused by slow-moving ejecta, this behavior should be more uniform from burst to burst. Such an analysis is beyond the scope of this work.

4.4. Burst Environment and Propagator Models

We now turn our attention to the issue of the circumburst medium. As discussed earlier, the radial profile of the burst environment affects the temporal decay below the cooling frequency (first three lines of eqs. [2] and [4]). In particular, the closure relationships (first three lines of eqs. [3] and [5]) are sufficiently different that we should be able to distinguish between the competing models for a well-sampled event like GRB 050820A.

First, we examine the X-ray data. As discussed previously (§ 4.3), the X-ray observations in phase 2 require invoking mild energy injection to explain the shallower than expected decay for $\nu(X) > \nu_c$. If we assume that the X-ray spectral index does not change from phase 2 to phase 3, then we find that $\alpha_{3,X}$ and $\beta_{3,X}$ satisfy the standard afterglow closure relation for $\nu_X > \nu_c$ (last

line of eqs. [3] and [5]). The corresponding values for the electron index are $p_{\alpha_{3,X}} = 2.3 \pm 0.1$ and $p_{\beta_{3,X}} = 2.40 \pm 0.08$.

Unlike the X-ray observations, the optical bands typically probe frequencies below the cooling frequency, where the closure relations are different for different circumburst media (third line of eqs. [3] and [5]). We have shown already in § 4.3 that the optical data in phase 2 are better fitted by a constant-density medium. We find that a constant-density medium is favored in the optical in phase 1b_{opt} and phase 3 as well. The only closure relation satisfied in phase 1b_{opt} is for an ISM with $\nu_m < \nu(\text{opt}) < \nu_c$ (third line of eq. [3]). The resulting p -values are $p_{\alpha_{1b,\text{opt}}} = 2.29 \pm 0.02$ and $p_{\beta_{1b,\text{opt}}} = 2.14 \pm 0.12$. We note that had we equated the BAT trigger time, T_{BAT} , with the onset of the burst (T_0), the temporal slope in phase 1b_{opt} would not have been consistent with any closure relation.

In phase 3, we cannot meaningfully constrain the optical spectral slope. However, using the X-ray–to–optical spectral slope in this phase, $\beta_{\text{ox},3} \approx 0.8$, we conclude that the optical data in this segment still fall below the cooling frequency. Based solely on the temporal decline then, we can rule out a windlike medium in this phase. The corresponding electron index ($p \approx 1.7 \pm 0.1$) would result in a divergent total energy. While this possibility has been addressed with more complicated electron energy distributions (see, e.g., Dai & Cheng 2001), we consider this possibility unlikely.

Taken together, the X-ray and optical data provide a consistent picture of the forward shock expanding into a constant-density medium. The late-time ($t_{\text{BAT}} > 1$ week) radio observations, however, are inconsistent with this interpretation. For a constant-density medium, the peak flux density, $F_{\nu,\text{max}}$, should remain constant in time. This would predict, if we have correctly interpreted the optical peak as the forward shock (§ 4.2), a similar peak ($F_{\nu,\text{max}} \approx 5$ mJy) in the radio at $t_{\text{BAT}} \approx 7$ days ($\nu_m \propto t^{-3/2}$). This is well above the VLA detection limit at this epoch, yet we only measure $F_{\nu} \approx 100$ μ Jy. While the energy injection phase will delay the arrival of ν_m in the radio ($\nu_m^{\text{inject}} \propto t^{-3/2} t^{3(s-1)/2(7+s)}$), our radio limits extend out to 2 months after the burst. It would be very difficult, if not impossible, to delay the peak this long. Furthermore, during the energy injection phase, the peak flux increases with time ($F_{\nu,\text{max}}^{\text{inject}} \propto t^{3(s-1)/(7+s)}$). Thus, we would expect to see rising emission earlier relative to the peak, counteracting the delay of the peak radio flux.

One explanation for the lack of a bright, late-time radio afterglow is an early jet break ($t \lesssim 1$ day), as was invoked for GRB 990123 (Kulkarni et al. 1999). However, we find no evidence for a jet break in the optical or X-ray light curves out to at least 17 days after the burst (see § 4.5).

Another possibility, invoked to explain the relatively low late-time radio flux from GRB 050904, is a high ambient density (Fraile et al. 2006). In the case of GRB 050904, it was argued that the large density raised the self-absorption frequency, ν_a , above the radio observing bands. This greatly suppresses the radio flux, for the spectrum in this regime is proportional to ν^2 (first line of eq. [1]). There is no evidence in the radio data for an optically thick spectrum, although spectral data are sparse at late times. Furthermore, broadband modeling of this event (§ 4.5) rules out a high ambient density for typical values of the microphysical parameters ϵ_e and ϵ_B . We therefore consider this explanation unlikely.

Alternatively, a natural explanation for the low radio flux at late times is a windlike medium. In a windlike medium, the forward shock peak flux density declines in time as $F_{\nu,\text{max}} \propto t^{-3/2}$. The decreasing peak flux counteracts the rising synchrotron emission, suppressing any late-time radio data. This is of course inconsistent

with our X-ray and optical data, which strongly favor a constant-density medium. One can imagine a scenario in which the environment near the burst (the regime sampled predominantly by the X-ray and optical data) is approximately constant in density, while the outer regions (sampled by the radio at later times) have a windlike profile. However, without a physical justification for such a density profile, this remains little more than speculation. The lack of a bright radio afterglow remains a puzzling aspect of GRB 050820A.

4.5. Geometry and Energetics

Using the high-energy fluence derived from *Konus-Wind* (§ 2.1.2), we calculate that the total isotropic energy release in the prompt emission was $E_{\gamma,\text{iso}} = 8.3_{-1.1}^{+2.5} \times 10^{53}$ ergs (assuming a redshift of $z = 2.615$; Prochaska et al. 2005; Ledoux et al. 2005). This makes GRB 050820A one of the most energetic events (in terms of $E_{\gamma,\text{iso}}$) for which a redshift has been measured (Amati 2006).

However, only a fraction of the explosion energy is converted into prompt emission via internal dissipation. The rest remains in the kinetic energy of the outflow, powering the forward shock and hence the afterglow. We can estimate the kinetic energy of the afterglow ($E_{\text{KE,iso}}$) by examining the X-ray emission at $t_{\text{BAT}} > 10$ hr (Freedman & Waxman 2001). At this point, the X-rays should be above the cooling frequency. The flux density is then independent of ambient density and only weakly dependent on ϵ_B . A joint fit of the phase 3 optical and X-ray data (after the energy injection has stopped and the system has returned to adiabatic expansion) constrains the electron energy index: $p = 2.34 \pm 0.06$. If we take typical values for ϵ_e (0.1–0.3) and ϵ_B (0.01–0.1; Yost et al. 2003), we find that $15 \lesssim E_{\text{KE,iso},52} \lesssim 100$.

For an accurate accounting of the total energy emitted by this event, however, we must determine the degree of collimation of the emission. We therefore examine all of the temporal breaks in the optical and X-ray light curves to determine which one (if any) shows an achromatic steepening to the t^{-p} decay expected from a jet (Sari et al. 1999). The only plausible candidate is the transition from phase 3 to 4 in the optical light curve. The steepening here is achromatic (i.e., it is seen in all three *HST* filters) and much too large to be explained solely by the cooling frequency passing through the optical bands (although this may have occurred as well). Any contribution from an underlying host galaxy would only further steepen the decay in phase 4.

With only one observation, it is impossible to constrain the postbreak decay index. Instead, we assume that the postbreak decay has a power-law index $\alpha = p \approx 2.34$ (see above). We then find $t_{\text{jet}} = 18 \pm 2$ days. This result is consistent with our X-ray observations, which put a lower limit on the jet break time of $t_{\text{jet}} \gtrsim 17$ days.

We note that the jet break time we have inferred for GRB 050820A is extremely large. In the host galaxy reference frame, the break occurs at $t_{\text{jet}}^{\text{host}} \approx 5$ days, a factor of 3 larger than any jet break seen in the pre-*Swift* era (Zeh et al. 2006). In this respect, too, GRB 050820A is a strong outlier.

To convert the jet break times to a range of opening angles, we use the relation (Sari et al. 1999)

$$\theta = 0.161 \left(\frac{t_j}{1+z} \right)^{3/8} \left(\frac{n\eta_\gamma}{E_{\gamma,\text{iso},52}} \right)^{1/8}. \quad (11)$$

Here η_γ is the fraction of the total energy converted to prompt γ -ray emission. The only remaining unknown in equation (11) is the ambient density, n . Using the ratio of the X-ray and optical data, as well as the canonical values of ϵ_e and ϵ_B , we find that the

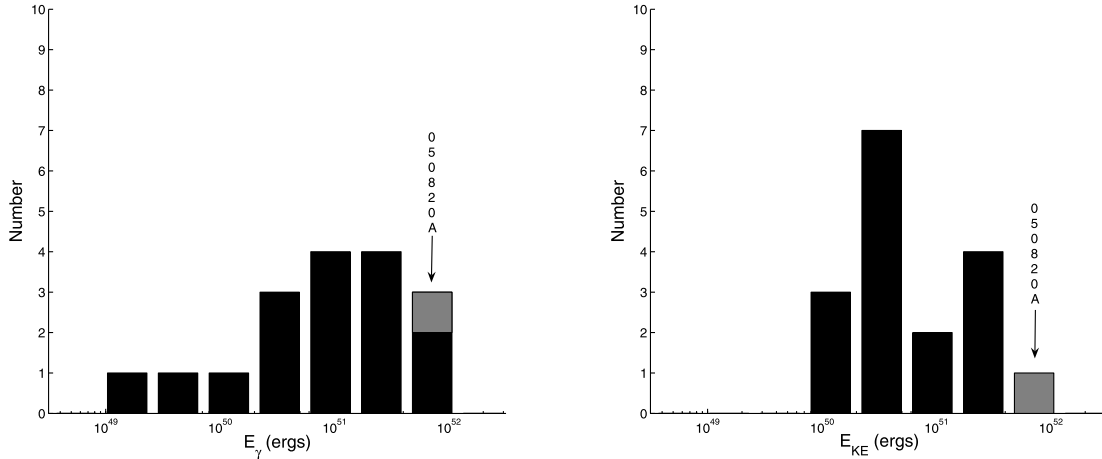


FIG. 8.—Total energy release of GRB 050820A. *Left*: Collimation-corrected energy release in the prompt emission (E_γ) of a sample of cosmological GRBs, including GRB 050820A. *Right*: Collimation-corrected blast wave energy (E_{KE}) for the same sample (Berger et al. 2001, 2003b, 2004; Yost et al. 2003; Panaitescu & Kumar 2002; Chevalier et al. 2004; Soderberg et al. 2004).

density of the burst must be low: $n \leq 1 \text{ cm}^{-3}$. Afterglow modeling of the late-time optical and X-ray data (phase 3, after any continued energy injection has ceased and the shock expands adiabatically) using the technique of Yost et al. (2003) confirms this result: $n \lesssim 0.1$.

Combining the above results, we find that the opening angle is constrained to fall between $6^\circ.8 \lesssim \theta \lesssim 9^\circ.3$, corresponding to a beaming factor $f_b \equiv 1 - \cos \theta \approx 10^{-2}$. While the opening angle is large for a long-soft burst, there are several comparable events in the pre-*Swift* sample (Zeh et al. 2006). The total collimation-corrected energy emitted in γ -rays (E_γ) from GRB 050820A is therefore $7.5^{+6.7}_{-2.4} \times 10^{51}$ ergs. The corresponding value for the blast wave energy (E_{KE}) is $5.2^{+7.9}_{-4.1} \times 10^{51}$ ergs.

Ghirlanda et al. (2004a) have demonstrated an empirical relation between E_γ and the peak energy of the prompt emission spectrum in the GRB rest frame (E_p^{rest}). GRB 050820A is more energetic than any of the 37 bursts considered in their sample (in terms of E_γ) and therefore proves an interesting test case for the so-called Ghirlanda relation. Using our calculated value of E_γ , Ghirlanda predicts $E_p^{\text{rest}} = 2.0^{+2.5}_{-1.2}$ MeV. This is marginally consistent with the actual value of $E_p^{\text{rest}} = 1.3^{+0.3}_{-0.2}$ MeV derived from the *Konus-Wind* data set.

In Figure 8 we plot a histogram of E_γ and E_{KE} for the ~ 15 long-soft cosmological bursts for which both quantities have been derived. We have not included the most nearby events (GRB 980425, GRB 031203, and GRB 060218) in our analysis, as these events released significantly less energy than the typical cosmological GRB (Soderberg et al. 2006). Soderberg et al. (2004) have shown that, with the exception of the most nearby events, the sum of E_γ and E_{KE} is clustered around 2×10^{51} ergs. GRB 050820A is clearly an overenergetic exception, an order of magnitude more energetic than this sample. In fact, it would require the direct conversion of $\approx 10^{-2} M_\odot$ (with 100% efficiency) to release this much energy.

Finally, it is important to consider how robust our estimates of $E_{\text{KE,iso}}$, θ , and n are given that the standard afterglow model fails to explain the broadband behavior of GRB 050820A. We note that the opening angle is relatively insensitive to both variables (eq. [11]); factors of order unity will be greatly reduced by the $\frac{1}{8}$ exponent. It is difficult to conceive of a long-soft GRB environment where the ambient density is less than 10^{-2} , and high densities would only increase the opening angle and thus the energy release.

5. CONCLUSIONS

GRB 050820A joins a select sample of events with simultaneous observations in the γ -ray and optical bands, and an even smaller group with contemporaneous X-ray observations as well. Such events have led to fundamental advances in our understanding of GRBs, including the discovery of a reverse shock optical flash from GRB 990123 (Akerlof et al. 1999) and possibly from GRB 050904 (Boër et al. 2006). The early-time optical emission from GRB 041219A also showed a bright optical flash, but the rise was correlated with an accompanying peak of γ -ray emission, suggesting a common origin for the two components (Vestrand et al. 2005).

The early behavior of GRB 050820A is unlike either of these events. Vestrand et al. (2006) have shown that the contemporaneous optical emission is well described as the sum of two components: one proportional to the prompt γ -ray emission and one smoothly varying forward shock term. While the γ -ray component is important for $t_{\text{BAT}} < 300$ s, the optical peak at $t_{\text{BAT}} \approx 600$ s is dominated by emission from the external shock region. Furthermore, the postpeak decay rate is inconsistent with reverse shock emission. Instead, we interpret this as the forward shock peak frequency passing through the optical bands. This is not unlike what was seen in the optical for GRB 060124 (Romano et al. 2006), although the time resolution in the prompt phase was much poorer than for this burst. The contemporaneous optical light curves of GRB 050319 (Quimby et al. 2006; Woźniak et al. 2005) and GRB 050401 (Rykoff et al. 2005) did not show this peak phase, but extrapolations to late times were consistent with the adiabatic expansion of a forward shock. Another different behavior was seen in the early optical light curve of GRB 050801, which showed an extended plateau phase correlated with the X-ray emission, hinting at continued energy injection from a central engine refreshing the external shocks (Rykoff et al. 2006).

The contemporaneous X-ray emission, on the other hand, is the low-energy tail of the prompt emission. This behavior was also seen for GRB 060124 (Romano et al. 2006) and has been hinted at in the rapid decline in early X-ray light curves attributed to high-latitude emission (Liang et al. 2006), as well as the bright X-ray flares seen in many XRT light curves (Burrows et al. 2005a). It is clear then that, in marked contrast to the X-ray emission, contemporaneous optical emission exhibits a large diversity in behavior.

Unfortunately, the physical mechanism behind this diversity remains to be explained.

The issue of burst geometry is a particularly interesting one in the *Swift* era. The steep postbreak decay slope, seen simultaneously in multiple filters, makes GRB 050820A one of the most convincing examples of a beamed event in the *Swift* sample. The X-ray afterglow, however, is too faint at late times to provide broadband confirmation. In fact, very few *Swift* bursts, including those, like GRB 050408 (Foley et al. 2006), that have been followed for months, show signs of a jet break in the XRT light curve (Nousek et al. 2006).

Typical jet breaks in pre-*Swift* bursts occurred on timescales of several days (Zeh et al. 2006). Perna et al. (2003) predicted that *Swift* would detect bursts with wider opening angles than previous missions due to the increased sensitivity of the BAT. However, not a single *Swift* afterglow has shown a convincing jet break-like transition in multiple bandpasses (candidates include GRB 050525A and GRB 050801; for a more thorough discussion see Panaitescu et al. 2006 and references therein). While it may be that most jet breaks, like GRB 050820A, occur at late times, beyond the sensitivity of the XRT and most ground-based facilities, this is nonetheless troubling. On the one hand, few if any X-ray jet breaks were seen in pre-*Swift* bursts; all collimation angles were determined from optical (and sometimes radio) light curves. Conversely, given the large number of well-sampled XRT light curves and the fact that such fundamental results for GRB cosmology as the Ghirlanda relation rest on our picture of GRBs as aspherical events, this is clearly a matter that merits further investigation.

One consequence of the large opening angle associated with GRB 050820A is a correspondingly large burst and afterglow energy. In fact, of all of the bursts compiled in the Ghirlanda et al. (2004b) sample, GRB 050820A has the largest prompt energy release. And unlike GRB 990123 (Panaitescu & Kumar 2001), this large γ -ray energy was accompanied by a correspondingly large kinetic energy imparted to the afterglow. The only comparable event for which such energies could be determined was the high-redshift burst GRB 050904, which released a total energy of $\sim 10^{52}$ ergs (Tagliaferri et al. 2005; Frail et al. 2006). Given the large γ -ray fluence, similar events should have been easily detected by both *Swift* and previous GRB missions. And given the bright optical afterglow and the late jet break, such events are strongly favored for ground-based follow-up (i.e., redshift determination). The lack of a large sample of such events means that they must be relatively rare in the universe.

Like many other *Swift* GRBs, the X-ray light curve of GRB 050820A exhibits a phase of shallow decay incompatible with the standard forward shock model (Nousek et al. 2006). GRB 050820A is relatively unique, however, in that this epoch is also

well sampled in the optical. The seemingly simultaneous breaks in the optical light curve bolster the commonly held belief that this phase is caused by some form of refreshed shocks (Zhang et al. 2006). Coupled with the large gap between the precursor and the bulk of the prompt emission, the late-time energy injection poses fundamental challenges to any central engine model.

Finally, we return to the question of the radio afterglow. Radio observations typically probe low Lorentz factor ejecta ($\Gamma \sim 2-3$) at large distances from the central engine ($r \sim 10^{17}$ cm). The forward shock peak frequency reaches the radio much later than the optical or X-ray bands. Thus, radio emission is usually visible at later times than optical or X-ray emission and is well suited to study afterglows when the emission is isotropic (i.e., after the jet break) or even in some cases when the ejecta has slowed to Newtonian expansion (Berger et al. 2004). For this reason, late-time radio observations are considered the most accurate method for model-independent calorimetry. For GRB 050820A, this paradigm has broken down. The burst had a bright optical and X-ray afterglow but weak emission in the radio. It is hoped that further studies of such energetic GRBs in the *Swift* era will help to elucidate some of these puzzles.

We would like to thank the anonymous referee for helpful comments on this manuscript. S. B. C. and A. M. S. are supported by the NASA Graduate Student Research Program. E. B. is supported by NASA through Hubble Fellowship grant HST-HF-01171.01 awarded by STScI, which is operated by the Association of Universities for Research in Astronomy, Inc., for NASA, under contract NAS5-26555. A. G. acknowledges support by NASA through Hubble Fellowship grant HST-HF-01158.01 awarded by STScI. The *Konus-Wind* experiment is supported by Russian Space Agency contract and RFBR grant 06-02-16070. GRB research at Caltech is supported through NASA. This publication has made use of data obtained from the *Swift* interface of the High-Energy Astrophysics Archive (HEASARC), provided by NASA's Goddard Space Flight Center. This publication makes use of data products from the Two Micron All Sky Survey, which is a joint project of the University of Massachusetts and the Infrared Processing and Analysis Center/California Institute of Technology, funded by the National Aeronautics and Space Administration and the National Science Foundation. The Digitized Sky Survey was produced at the Space Telescope Science Institute under US Government grant NAG W-2166. The images of these surveys are based on photographic data obtained using the Oschin Schmidt Telescope on Palomar Mountain and the UK Schmidt Telescope. The plates were processed into the present compressed digital form with the permission of these institutions.

REFERENCES

- Akerlof, C., et al. 1999, *Nature*, 398, 400
 Amati, L. 2006, *MNRAS*, in press (astro-ph/0601553)
 Aptekar, R. L., et al. 1995, *Space Sci. Rev.*, 71, 265
 Aslan, Z., et al. 2005, *GRB Circ.*, 3896, 1
 Band, D., et al. 1993, *ApJ*, 413, 281
 Barthelmy, S. D., et al. 2005, *Space Sci. Rev.*, 120, 143
 Berger, E., Kulkarni, S. R., & Frail, D. A. 2003a, *ApJ*, 590, 379
 ———. 2004, *ApJ*, 612, 966
 Berger, E., et al. 2001, *ApJ*, 556, 556
 ———. 2003b, *Nature*, 426, 154
 ———. 2005, *Nature*, 438, 988
 Bikmaev, I., et al. 2005, *GRB Circ.*, 3853, 1
 Boër, M., Atteia, J. L., Damerdy, Y., Gendre, B., Klotz, A., & Stratta, G. 2006, *ApJ*, 638, L71
 Briggs, M. S., et al. 1999, *ApJ*, 524, 82
 Burrows, D. N., et al. 2005a, *Science*, 309, 1833
 ———. 2005b, *Space Sci. Rev.*, 120, 165
 Cenko, S. B., & Fox, D. B. 2005, *GRB Circ.*, 3834, 1
 Cenko, S. B., et al. 2006, *PASP*, in press (astro-ph/0608323)
 Chester, M., Page, M., Roming, P., Marshall, F., Boyd, P., Angelini, L., Greiner, J., & Gehrels, N. 2005, *GRB Circ.*, 3838, 1
 Chevalier, R. A., & Li, Z.-Y. 2000, *ApJ*, 536, 195
 Chevalier, R. A., Li, Z.-Y., & Fransson, C. 2004, *ApJ*, 606, 369
 Cummings, J., et al. 2005a, *GRB Circ.*, 3835, 1
 ———. 2005b, *GRB Circ.*, 3858, 1
 Cusumano, G., et al. 2006, *Nature*, 440, 164
 Dai, Z. G., & Cheng, K. S. 2001, *ApJ*, 558, L109
 Dai, Z. G., Liang, E. W., & Xu, D. 2004, *ApJ*, 612, L101
 Dickey, J. M., & Lockman, F. J. 1990, *ARA&A*, 28, 215
 Falcone, A. D., et al. 2006, *ApJ*, 641, 1010

- Firmani, C., Avila-Reese, V., Ghisellini, G., & Ghirlanda, G. 2006, MNRAS, in press (astro-ph/0605430)
- Foley, R. J., et al. 2006, ApJ, 645, 450
- Ford, L. A., et al. 1995, ApJ, 439, 307
- Fox, D. B., & Cenko, S. B. 2005, GRB Circ., 3829, 1
- Frail, D. A., Kulkarni, S. R., Nicastro, S. R., Feroci, M., & Taylor, G. B. 1997, Nature, 389, 261
- Frail, D. A., et al. 2001, ApJ, 562, L55
- . 2006, ApJ, 646, L99
- Freedman, D. L., & Waxman, E. 2001, ApJ, 547, 922
- Friedman, A. S., & Bloom, J. S. 2005, ApJ, 627, 1
- Frontera, F., et al. 2000, ApJS, 127, 59
- Fruchter, A. S., & Hook, R. N. 2002, PASP, 114, 144
- Fukugita, M., Shimasaku, K., & Ichikawa, T. 1995, PASP, 107, 945
- Gal-Yam, A., et al. 2004, ApJ, 609, L59
- Gehrels, N., et al. 2004, ApJ, 611, 1005
- . 2005, Nature, 437, 851
- Ghirlanda, G., Ghisellini, G., & Lazzati, D. 2004a, ApJ, 616, 331
- Ghirlanda, G., Ghisellini, G., Lazzati, D., & Firmani, C. 2004b, ApJ, 613, L13
- Goodman, J. 1997, NewA, 2, 449
- Granot, J., & Sari, R. 2002, ApJ, 568, 820
- Haislip, J. B., et al. 2006, Nature, 440, 181
- Henden, A. 2005, GRB Circ., 3845, 1
- Kann, D. A., Kloze, S., & Zeh, A. 2006, ApJ, 641, 993
- Katz, J. I., & Piran, T. 1997, ApJ, 490, 772
- Kent, S. M. 1985, PASP, 97, 165
- Khamitov, I., et al. 2005, GRB Circ., 3864, 1
- Kobayashi, S. 2000, ApJ, 545, 807
- Kulkarni, S. R., et al. 1999, ApJ, 522, L97
- Kumar, P., & Panaitescu, A. 2000, ApJ, 541, L51
- Lazzati, D. 2005, MNRAS, 357, 722
- Ledoux, C., et al. 2005, GRB Circ., 3860, 1
- Li, W., Jha, S., Filippenko, A. V., Bloom, J. S., Pooley, D., Foley, R. J., & Perley, D. A. 2006, PASP, 118, 37
- Liang, E. W., et al. 2006, ApJ, 646, 351
- Lyutikov, M., & Blandford, R. 2003, preprint (astro-ph/0312347)
- Lyutikov, M., & Usov, V. V. 2000, ApJ, 543, L129
- MacLeod, C., & Nysewander, M. 2005, GRB Circ., 3863, 1
- McBreen, S., Hanlon, L., McGlynn, S., McBreen, B., Foley, S., Preece, R., von Kienlin, A., & Williams, O. R. 2006, A&A, 455, 433
- Mészáros, P., & Rees, M. J. 2000, ApJ, 530, 292
- Metzger, M. R., Djorgovski, S. G., Kulkarni, S. R., Steidel, C. C., Adelberger, K. L., Frail, D. A., Costa, E., & Frontera, F. 1997, Nature, 387, 878
- Nousek, J. A., et al. 2006, ApJ, 642, 389
- O'Brien, P. T., et al. 2006, ApJ, 647, 1213
- Paczynski, B. 1986, ApJ, 308, L43
- Page, K. L., Beardmore, A. P., Goad, M. R., Kennea, J. A., Burrows, D. N., Marshall, F., & Smale, A. 2005a, GRB Circ., 3837, 1
- Page, M., et al. 2005b, GRB Circ., 3830, 1
- Pal'shin, V., & Frederiks, D. 2005, GRB Circ., 3852, 1
- Panaitescu, A., & Kumar, P. 2001, ApJ, 554, 667
- . 2002, ApJ, 571, 779
- Panaitescu, A., Mészáros, P., Burrows, D., Nousek, J., Gehrels, N., O'Brien, P., & Willingale, R. 2006, MNRAS, 369, 2059
- Pei, Y. C. 1992, ApJ, 395, 130
- Perna, R., Sari, R., & Frail, D. 2003, ApJ, 594, 379
- Piran, T. 2005, Rev. Mod. Phys., 76, 1143
- Price, P. A., et al. 2002, ApJ, 572, L51
- Prochaska, J. X., Bloom, J. S., Wright, J. T., Butler, R. P., Chen, H. W., Vogt, S. S., & Marcy, G. W. 2005, GRB Circ., 3833, 1
- Quimby, R. M., et al. 2006, ApJ, 640, 402
- Ramirez-Ruiz, E., MacFadyen, A. I., & Lazzati, D. 2002, MNRAS, 331, 197
- Rees, M. J., & Mészáros, P. 1998, ApJ, 496, L1
- . 2000, ApJ, 545, L73
- Rhoads, J. E. 1999, ApJ, 525, 737
- Romano, P., et al. 2006, A&A, 456, 917
- Roming, P. W. A., et al. 2005, Space Sci. Rev., 120, 95
- Rybicki, G., & Lightman, A. 1979, Radiative Processes in Astrophysics (New York: Wiley)
- Rykoff, E. S., et al. 2005, ApJ, 631, L121
- . 2006, ApJ, 638, L5
- Sari, R., & Mészáros, P. 2000, ApJ, 535, L33
- Sari, R., & Piran, T. 1999a, ApJ, 517, L109
- . 1999b, ApJ, 520, 641
- Sari, R., Piran, T., & Halpern, J. P. 1999, ApJ, 519, L17
- Sari, R., Piran, T., & Narayan, R. 1998, ApJ, 497, L17
- Schlegel, D. J., Finkbeiner, D. P., & Davis, M. 1998, ApJ, 500, 525
- Sirianni, M., et al. 2005, PASP, 117, 1049
- Skrutskie, M. F., et al. 2006, AJ, 131, 1163
- Soderberg, A. M., et al. 2004, Nature, 430, 648
- . 2006, Nature, 442, 1014
- Tagliaferri, G., et al. 2005, A&A, 443, L1
- Thuan, T. X., & Gunn, J. E. 1976, PASP, 88, 543
- Tody, D. 1986, Proc. SPIE, 627, 733
- Vaughan, S., et al. 2006, ApJ, 638, 920
- Vestrand, W. T., et al. 2005, Nature, 435, 178
- . 2006, Nature, 442, 172
- Waxman, E., & Mészáros, P. 2003, ApJ, 584, 390
- Woodsley, S. E. 1993, ApJ, 405, 273
- Woźniak, P. R., Vestrand, W. T., Wren, J. A., White, R. R., Evans, S. M., & Casper, D. 2005, ApJ, 627, L13
- Wren, J., Vestrand, W. T., Woźniak, P., Evans, S., & White, R. 2005, GRB Circ., 3836, 1
- Yost, S. A., Harrison, F. A., Sari, R., & Frail, D. A. 2003, ApJ, 597, 459
- Zeh, A., Kloze, S., & Kann, D. A. 2006, ApJ, 637, 889
- Zhang, B., Fan, Y. Z., Dyks, J., Kobayashi, S., Mészáros, P., Burrows, D. N., Nousek, J. A., & Gehrels, N. 2006, ApJ, 642, 354